JGR Space Physics

RESEARCH ARTICLE
10.1029/2021JA030118

The Height-Dependent Delayed Ionospheric Response to Solar EUV

Erik Schmölter[1], Frank Heymann[1], Christian von Savigny[2], and Jens Berdermann[1]

[1]German Aerospace Center, Institute for Solar-Terrestrial Physics, Neustrelitz, Germany, [2]Institute of Physics, University of Greifswald, Greifswald, Germany

Key Points:

- A response to solar 27-day signatures is observed in ionosonde N_e height profiles and successfully reproduced with a Thermosphere-Ionosphere-Electrodynamics General Circulation Model simulation
- Height-dependent variations of the delayed ionospheric response are driven by the respective contributions of O^+ and O_2^+
- Transport processes have a significant impact on the 27-day signatures of neutral and ionized parts in the upper atmosphere

Correspondence to:
E. Schmölter,
Erik.Schmoelter@dlr.de

Citation:
Schmölter, E., Heymann, F., von Savigny, C., & Berdermann, J. (2022). The height-dependent delayed ionospheric response to solar EUV. *Journal of Geophysical Research: Space Physics*, *127*, e2021JA030118. https://doi.org/10.1029/2021JA030118

Received 9 NOV 2021
Accepted 10 MAR 2022

Abstract Based on the analysis of electron density N_e profiles (Grahamstown ionosonde), a case study of the height-dependent ionospheric response to two 27-day solar rotation periods in 2019 is performed. A well-defined sinusoidal response is observed for the period from 27 April 2019 to 24 May 2019 and reproduced with a Thermosphere-Ionosphere-Electrodynamics General Circulation Model simulation. The occurring differences between model and observations as well as the driving physical and chemical processes are discussed based on the height-dependent variations of N_e and major species. Further simulations with an artificial noise free sinusoidal solar flux input show that the N_e delay is defined by contributions due to accumulation of O^+ at the N_e peak (positive delay) and continuous loss of O_2^+ in the lower ionosphere (negative delay). The neutral parts' 27-day signatures show stronger phase shifts. The time-dependent and height-dependent impact of the processes responsible for the delayed ionospheric response can therefore be described by a joint analysis of the neutral and ionized parts. The return to the initial ionospheric state (and thus the loss of the accumulated O^+) is driven by an increase of downward transport in the second half of the 27-day solar rotation period. For this reason, the neutral vertical winds (upwards and downwards) and their different height-dependent 27-day signatures are discussed. Finally, the importance of a wavelength-dependent analysis, statistical methods (superposed epoch analysis), and coupling with the middle atmosphere is discussed to outline steps for future analysis.

1. Introduction

The ionospheric plasma in the upper atmosphere is created and affected by complex interactions that are driven, among others, by solar and geomagnetic activity (Rishbeth & Mendillo, 2001). The solar radiation, and more specifically the solar extreme ultraviolet (EUV) radiation, is absorbed at different heights and initiates ionization and dissociation processes depending on the existing composition. The creation of plasma is balanced by various recombination processes, which also occur at different heights. Additional interactions (e.g., composition changes due to transport processes) affect the ionospheric plasma further (Kelley, 2009). The maximum of the resulting plasma density profile, the so-called F region, occurs at heights from 150 to 500 km and consists almost entirely of O^+. At lower heights from 90 to 150 km, the ionospheric plasma is dominated by NO^+ and O_2^+. The different ionization processes that cause this plasma distribution are dependent on the wavelength of the solar EUV radiation (Kelley, 2009). Thus, variations in the solar spectrum are also associated with height-dependent ionospheric variability.

A significant solar activity variation is the 27-day solar rotation period, which can cause observable signatures in the ionosphere (Ma et al., 2012). Furthermore, a delay between the solar and ionospheric signatures was shown for this variation by several studies (Afraimovich et al., 2008; Jakowski et al., 1991, 2002; Lee et al., 2012; Min et al., 2009; Oinats et al., 2008; Ren et al., 2018; Schmölter et al., 2018Schmölter, Berdermann, Jacobi, & Jakowski, 2020; Schmölter, Berdermann, Jakowski, & Jacobi, 2020; Titheridge, 1973; Zhang & Holt, 2008) and investigated based on model simulations (Ren et al., 2018, 2019, 2020; Vaishnav et al., 2018, 2019). The reported delays range from a few hours to several days, depending on the selected observable and methods. Schmölter et al. (2021) and Vaishnav et al. (2021) observed different delays based on calculations using solar EUV proxies and measurements. Different delays were also shown for different ionospheric parameters (Schmölter, Berdermann, Jacobi, & Jakowski, 2020; Schmölter, Berdermann, Jakowski, & Jacobi, 2020). These delays between solar and ionospheric parameters are either calculated by applying the difference between occurring maxima of the 27-day solar rotation period or by applying the lag of the corresponding cross-correlation. The second method is more reliable for measurement data (Schmölter et al., 2021), while the first method is more appropriate for model simulations allowing a comprehensive analysis of temporal variations.

The delayed ionospheric response and its variability (e.g., spatial, seasonal, or annual variations) are driven by immediate ionization of O and slower recombination to O_2 and N_2 (Ren et al., 2018, 2019). If an imbalance between these processes in favor of the ion production occurs (e.g., during enhanced solar activity) then an accumulation of O^+ may be observed past the maximum of the solar activity. The ionization of O can be further enhanced due to the photodissociation of O_2 above 250 km and molecular diffusion (Jakowski et al., 1991; Vaishnav et al., 2021). Furthermore, changes of the eddy diffusion affect the delayed ionospheric response significantly (Vaishnav et al., 2021).

Recent studies investigated the delayed ionospheric response with upper atmosphere models to improve the understanding of the underlying processes. The delay was studied with the Coupled Thermosphere Ionosphere Plasmasphere Electrodynamics Model (CTIPe) by Vaishnav et al. (2018, 2020, 2021) to analyze the features of temporal and spatial variations, the response to different solar activity and the role of the eddy diffusion. Vaishnav et al. (2021) confirmed and discussed the increase of the delayed ionospheric response with increasing solar activity, which was indicated in analysis based on observations by Schmölter, Berdermann, Jacobi, & Jakowski, 2020; Schmölter, Berdermann, Jakowski, & Jacobi, 2020. In addition, Vaishnav et al. (2021) investigated the increase of the delayed ionospheric response with decreasing eddy diffusion and vice versa. This observed increase of the delay is due to the slow mixing of the plasma (small eddy diffusion) and the decreased recombination rates. Thus, further enhancing the time difference between solar activity changes and corresponding ionospheric response. Ren et al. (2018) investigated the delayed response of the F region in more detail based on electron density measurements of the Challenging Minisatellite Payload (CHAMP) and EUV measurements of the Solar Extreme Ultraviolet Experiment (SEE) instrument on board the Thermosphere Ionosphere Mesosphere Energetic and Dynamics (TIMED). Simulations of the analyzed periods with the Thermosphere-Ionosphere-Electrodynamics General Circulation Model (TIE-GCM) were in good agreement with the observational results and revealed that geomagnetic activity affects the delay (Ren et al., 2018). Further TIE-GCM simulations by Ren et al. (2019) investigated the delayed thermospheric temperature response to the 27-day solar rotation period and found a delay driven by the balance of heating and cooling rates. The different responses of O and N_2 to the 27-day solar rotation period were also investigated with TIE-GCM simulations revealing that these delays are driven by the barometric effect and dynamic processes (Ren et al., 2020).

Thus, different responses to the 27-day solar rotation period were investigated for different thermospheric and ionospheric parameters, which are controlled by height-dependent processes. However, the understanding of the interactions between these processes needs to be improved and especially the role of transport processes and the coupling of thermosphere and ionosphere requires further studies. For this purpose, the height-dependent response is investigated in detail in the present study.

Schmölter et al. (2021) investigated the response of the ionosphere to two well-defined 27-day solar rotation periods in 2019 with different National Aeronautics and Space Administration (NASA) Global-scale Observations of the Limb and Disk (GOLD) measurements and International GNSS Service (IGS) total electron content (TEC) maps. The study reported good correlations between the solar radio flux index F10.7 as well as the GOLD solar EUV proxy Q_{EUV} with TEC at a location in the observation area of GOLD. The ionospheric response to the solar activity changes was not immediate in both cases and thus delays are observed in each period. The present study investigates the two well-defined 27-day solar rotation periods analyzed by Schmölter et al. (2021) from 27 April 2019 to 24 May 2019 and from 23 May 2019 to 19 June 2019 in more detail. For this purpose, ionosonde data are applied to extend the delay analysis with height-dependent profiles. The analysis is complemented with TIE-GCM simulations to discuss the observed height-dependent variations of the delay. More specifically, this study analyses the delayed ionospheric response from approximately 100 to 300 km covering the lower ionosphere and the peak of the ionospheric plasma density profile. The estimated, height-dependent delays are of interest for a better understanding of the ionosphere but also the mesosphere-lower thermosphere (MLT) system, and characterize the upper atmosphere response to solar activity changes in more detail.

2. Data

In a previous study, two 27-day solar rotation periods from 27 April 2019 to 24 May 2019 and from 23 May 2019 to 19 June 2019 have been analyzed with NASA GOLD data and IGS TEC maps (Schmölter et al., 2021). The reported delays estimated by comparison of peak times and cross-correlation were in good agreement with other

studies of the delay (e.g., Ren et al., 2018, 2019, 2020, 2021; Schmölter, Berdermann, Jacobi, & Jakowski, 2020; Schmölter, Berdermann, Jakowski, & Jacobi, 2020). This study further analyses these periods and adapts the methods used in Schmölter et al. (2021). In contrast to the previous study, the solar radio flux index F10.7 is used in this study instead of the GOLD solar EUV proxy Q_{EUV} for a better comparability between observational and model results.

2.1. Solar Radio Flux Index F10.7

The GOLD solar EUV proxy Q_{EUV} correlates better than the solar radio flux index F10.7 with the observed TEC variations during the two 27-day solar rotation periods from 27 April 2019 to 24 May 2019 and from 23 May 2019 to 19 June 2019 (Schmölter et al., 2021). This better correlation results in a more reliable delay estimation (Schmölter et al., 2021). Nevertheless, the F10.7 is applied to the delay calculations in the present study since observational results are compared to TIE-GCM runs using F10.7 as input. This approach ensures that the differences between Q_{EUV} and F10.7 do not affect the results of this study. Furthermore, no improvements are expected with respect to the use of solar EUV data with TIE-GCM because of the variations in the measured spectrum and the uncertainties of the cross-sections applied, which are larger than the uncertainties of the F10.7-based modeling approach (Solomon, 2005). The analysis and discussion of the influence of different solar EUV spectra or proxies were done by other studies (Vaishnav et al., 2020) and are not part of this work.

F10.7 is a commonly used index describing the solar activity at a wavelength of 10.7 cm. The index describes the solar variability in general and is used as a proxy for solar radiation at wavelengths which are difficult to measure (Tapping, 2013). Calculations of the delayed ionospheric response based on F10.7 have been presented in several studies (e.g., Afraimovich et al., 2008; Jakowski et al., 1991, 2002; Lee et al., 2012; Min et al., 2009; Oinats et al., 2008; Zhang & Holt, 2008) providing a good basis for comparison in further investigations. F10.7 data are part of the NASA/GSFC's OMNI data set that is provided through the OMNIWeb interface (NASA, 2021).

2.2. Mg II Solar Index

The Mg II solar activity index is the solar irradiance ratio of the unresolved Mg II doublet at 280 nm and the nearby continuum irradiance (DeLand & Cebula, 1993) and is a well-suited proxy for the solar EUV radiation (Viereck et al., 2001). The 11-year solar cycle variation as well as the 27-day solar rotation period are observed with the index (DeLand & Cebula, 1993; Snow et al., 2014; Viereck et al., 2001). The composite Mg II index provided by the Institute of Environmental Physics (IUP) at the University of Bremen combines the Mg II data from different instruments including the Global Ozone Monitoring Experiment (GOME), Scanning Imaging Absorption Spectrometer for Atmospheric Chartography (SCIAMACHY), and GOME-2. The data provided are available from 1978 to the present and thus, like F10.7, are suitable for long-term studies. The composite Mg II index was also confirmed to be very reliable for long-term studies of the delayed ionospheric response to solar activity (Vaishnav et al., 2019). For this reason, it is used for statistical analysis of multiple 27-day solar rotation periods using superposed epoch analysis (SEA) in this study.

The Bremen Mg II composite data as well as the separate measurements are provided through the UV Satellite Data and Science Group (UVSat) web page (IUP, 2021).

2.3. Kp Index

The delayed ionospheric response to the 27-day solar rotation period is affected by geomagnetic activity (Ren et al., 2018; Schmölter, Berdermann, Jacobi, & Jakowski, 2020; Schmölter, Berdermann, Jakowski, & Jacobi, 2020) and therefore its impact has to be taken into account in the present study. Weak geomagnetic activity occurred during the selected periods with a significant impact on the thermospheric composition (Cai et al., 2020, 2021). Thus, an impact on ionospheric parameters and the response to the 27-day solar rotation period can be expected as well. The Kp index describes the disturbances in the horizontal component of Earth's magnetic field on a global scale (Matzka, Stolle, et al., 2021) and is applied in the present study. The global Kp index is provided by the German Research Centre for Geosciences in Potsdam (GFZ, 2021; Matzka, Bronkalla, et al., 2021).

2.4. Ionosonde Electron Density Height Profiles

Schmölter et al. (2021) estimated the delayed ionospheric response during the two 27-day solar rotation periods from 27 April 2019 to 24 May 2019 and from 23 May 2019 to 19 June 2019 with vertical TEC data. Delay analyses based on this ionospheric observable have shown different spatial and temporal variations of the delay (e.g., Schmölter et al., 2018) but a height-dependent analysis is naturally not possible with an integral measurements of the electron density N_e profile. N_e height profiles by ionosondes, on the other hand, allow such an analysis. Ionospheric parameters derived from these profiles, e.g., F2 layer peak electron density NmF2 or critical frequency foF2, have been used in studies of the delayed ionospheric response (Oinats et al., 2008; Schmölter et al., 2018) and generally the results correspond to those based on TEC data. Occurring differences between the estimated delays, e.g., less pronounced seasonal variations of the delay based on TEC data, can be attributed to TEC describing the entire ionosphere including the plasmasphere and the selected N_e profile parameters describing only a single layer of the ionosphere (Schmölter et al., 2018). Because of these good agreements, the aim of this study is to extend the previous analysis based on TEC data by taking into account ionosonde data.

For the analysis all ionosonde stations from the Master Ionosonde Data Set (MIDS) are considered that are in the area observed by GOLD and that are in close proximity to the location (0°N and 0°E) analyzed by Schmölter et al. (2021). The absence of data gaps during the two 27-day solar rotation periods is another criterion for the selection. As a conclusion, the station Grahamstown is selected for the further analysis. This station is located at 33.3°S and 26.5°E in South Africa and operates since 1973 (McKinnell, 2008). The provided ionograms, which are generated using the measured tracings of reflected high frequency radio pulses, as well as the derived numerical values have a sampling rate of 15 min. This is sufficient for reliable calculation of the delayed ionospheric response. The National Oceanic and Atmospheric Administration's (NOAA) National Centers for Environmental Information (NCEI) provide real time ionograms as well as the archived data sets used in this study (NCEI, 2021).

For the analysis of electron density profiles and comparison to TIE-GCM simulations, only ionograms with an Assigned Quality Index (AQI) of 2 and 3 are applied (good and very good data). This does not guarantee to avoid errors and artifacts, but it significantly reduces the impact of unreliable data.

2.5. Thermosphere-Ionosphere-Electrodynamics General Circulation Model

TIE-GCM is a global three-dimensional numerical model for the coupled thermosphere/ionosphere (TI) system (Qian et al., 2014; Roble et al., 1988), that is developed at the National Center for Atmospheric Research (NCAR) High-Altitude Observatory (HAO). The model includes a self-consistent solution of the middle and low-latitude dynamo field and solves the three-dimensional momentum, energy, and continuity equations for neutral and ion species. This is realized with a semi-implicit, fourth-order, centered finite difference scheme. TIE-GCM provides accurate and self-consistent calculations for the TI system including different aeronomic parameters and minor species. The horizontal resolution of the model is 5° × 5° (optional 2.5° × 2.5°).

The model outputs (e.g., ionospheric parameters) are obtained as a function of independent variables: time t, latitude ϕ, longitude λ, and pressure interface z. These pressure P interfaces z are defined with the reference pressure P_0 of 5×10^{-5} Pa (Qian et al., 2014) according to

$$z = \ln \frac{P_0}{P}. \tag{1}$$

There are 29 (57 for horizontal resolution of 2.5° × 2.5°) pressure interfaces (from −7 to +7) that cover a height range from approximately 97 to 600 km. The geopotential height Z, which is of major importance for this study, is a dependent variable in TIE-GCM (Qian et al., 2014), that is defined at the lower boundary depending on semidiurnal migrating tide Z_{SD}, migrating diurnal tide Z_D, annual tide Z_A, nonmigrating semidiurnal tide Z_{nSD}, and nonmigrating diurnal tides Z_{nD} (Hagan & Forbes, 2002, 2003) according to

$$Z\,(z_{bot}) = Z_{SD} + Z_D + Z_A + Z_{nSD} + Z_{nD}. \tag{2}$$

The geopotential height $Z(z + \Delta z)$ at each pressure interface is calculated using the hydrostatic equation with gas constant R^*, neutral temperature T_n, acceleration of gravity g, and mean molecular mass $\overline{m}$ according to

$$Z(z + \Delta z) = \frac{\Delta z \cdot R^*}{g} \cdot \frac{T_n}{\overline{m}} \left(z + \frac{1}{2} \Delta z \right) + Z(z). \tag{3}$$

The geopotential height at the lower boundary (pressure interface of −7) is ∼96.37 km, the neutral temperature is set to 181 K, and the neutral zonal and meridional winds are 0 cm s^{-1}. These variables define the constant background field.

For this study, a semilogarithmic interpolation is applied in height to transform the model outputs dependent on geopotential heights from an irregular to a regular grid. The resulting model outputs depend on a new set of variables: time t, latitude ϕ, longitude λ, and geopotential height Z. This allows a height-dependent analysis of the different ionospheric parameters.

TIE-GCM calculates the major species (O, O_2, and N_2) using vertical molecular diffusion, vertical eddy diffusion, horizontal and vertical advection as well as production and loss due to chemical reactions (Cai et al., 2021; Qian et al., 2014; Sutton et al., 2015; Yu et al., 2021). The O^+ density is calculated according to the continuity equation considering transport due to neutral winds, transport due to ambipolar diffusion, $\mathbf{E} \times \mathbf{B}$ transport as well as production Q and loss L due to chemical reactions (Liu et al., 2016)

$$\frac{\partial n}{\partial t} - Q + L \cdot n = -\nabla (n \cdot \mathbf{v}_i) . \tag{4}$$

The ion velocity $\mathbf{v}_i$ combines the different transport processes in Equation 4. The ions of minor species and the electron density N_e are calculated assuming the photochemical equilibrium for ions other than O^+ using production and loss due to chemical reactions (Liu et al., 2016) and are related according to

$$N_e = n\left(O^+\right) + n\left(N_2^+\right) + n\left(N^+\right) + n\left(O_2^+\right) + n\left(NO^+\right) . \tag{5}$$

Lower boundary conditions also apply to these parameters. The vertical gradient of the O density is set to 0, the O_2 mixing ratio is set to 0.22, the N_2 mixing ratio is set to 0.78, and the photochemical equilibrium is assumed for O^+ (Qian et al., 2014). The auroral precipitation model of TIE-GCM is based on the model of high-latitude auroral processes by Roble and Ridley (1987), which allows to calculate ion and electron density variations due to auroral particle precipitation.

TIE-GCM provides adequate descriptions of density variations driven by the solar cycle, 27-day solar rotation period, and geomagnetic variations (Qian et al., 2009, 2014). The general circulation is also correctly described (Qian et al., 2009). Overall, TIE-GCM is well-suited for the aim of this study, but especially the impact of the lower boundary conditions has to be considered for the height-dependent analysis of the delayed ionospheric response. The model code, description, and documentation are provided by NCAR HAO through the official web page (HAO, 2021).

3. The Delayed Ionospheric Response Presented on the Basis of Electron Density Height Profiles

The temporal variation of the N_e profile at the station Grahamstown is shown in Figure 1. At ∼200 km pronounced peaks of the N_e profiles are observed with decreasing values at smaller and greater heights. In the second period (see Figure 1d), the N_e profile extends significantly beyond heights of 350 km on 6 days. There are also data gaps or unexpectedly high N_e values. These variations are due to wrong default traces in the ionograms, that are not identified with the defined AQI requirement. The first period (see Figure 1c), that is further analyzed, is not affected by similar irregularities. In addition, there is a strong decrease at all heights during 29 May 2019 that cannot be attributed to the observed solar and geomagnetic activity changes (see Figure 1b).

The first period in Figure 1c has stronger increases above 200 km during 2 May 2019, 11 May 2019, and 14 May 2019 which are due to enhanced geomagnetic activity (see Figure 1a). Thus, the thermospheric response to weak geomagnetic activity during that period (Cai et al., 2021) is also shown with the ionospheric response. Another increase during 7 May 2019 is due to enhanced solar activity (see Figure 1a). The increase during 11 May 2019 corresponds to the maximum of the respective 27-day solar rotation period. Both of these variations were reported for F10.7 but even more pronounced for the GOLD solar EUV proxy Q_{EUV} (Schmölter, Berdermann, Jacobi, & Jakowski, 2020; Schmölter, Berdermann, Jakowski, & Jacobi, 2020). The second period in Figure 1d has no significant increases and in general N_e is smaller compared to the first period. Starting 13 June 2019, N_e decreases noticeable above 200 km causing an apparent lowering of the profile. Nevertheless, a dependence

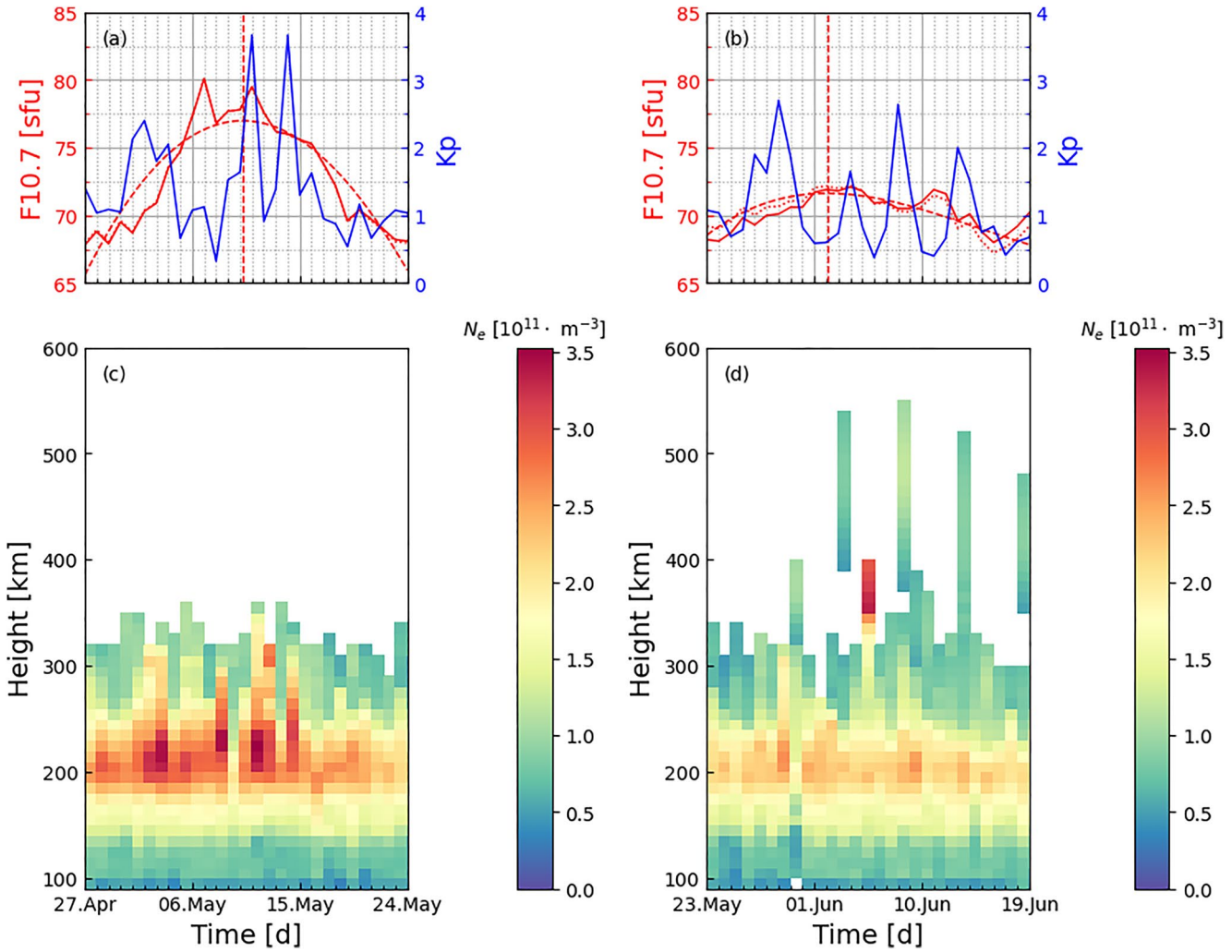

Figure 1. Solar radio flux index F10.7, Kp index, and electron density N_e profile at the station Grahamstown (33.3°S and 26.5°E) from 27 April 2019 to 24 May 2019 (a, c) and from 23 May 2019 to 19 June 2019 (b, d). Each bin represents the daily mean for a 10-km height level.

on the two 27-day solar rotation periods is indicated due to the enhancement of N_e (especially at the peak) in Figure 1c. For this reason, N_e at different heights has to be analyzed in more detail to extract the ionospheric response to the solar activity variations.

For the analysis of a N_e profile at specific heights, the methods by Schmölter et al. (2021) are applied. Each data set is first adjusted to remove the linear trend occurring during the two periods, then a basis spline interpolation for the time series is calculated and the peak of this result is estimated. This method allows a comparison of the solar and geomagnetic activity with the ionospheric state during well-defined 27-day solar rotation periods. The delay is estimated as the difference between the peak times. Figure 2 shows the results of these calculations for F10.7, Kp, and N_e at 130, 160, 190, and 220 km. The interpolated F10.7 time series during first period in Figure 2a has a well-defined and centered variation. During the second period in Figure 2b, the increase of F10.7 is smaller and the maximum occurs earlier. The first and second peaks are observed during 10 May 2019 and 2 June 2019. For interpolated N_e at 220 km (see Figures 2c and 2d), a correlation with F10.7 is observed with the maxima of N_e before the maxima of F10.7. At lower heights, the signature of the 27-day solar rotation period is less pronounced and the maxima of N_e occur increasingly later. For this reason, the correlation decreases and the delay increases. A similar behavior is observed for noninterpolated N_e and Kp. At 220 km, significant N_e increases are observed during enhanced Kp in the first period (see Figures 2a and 2c). These increases are considerably weaker at 190 km and are not observed at 160 and 130 km. As expected, the impact of solar and geomagnetic activity is decreasing with increasing distances from the N_e profile peak which is the region covering the major

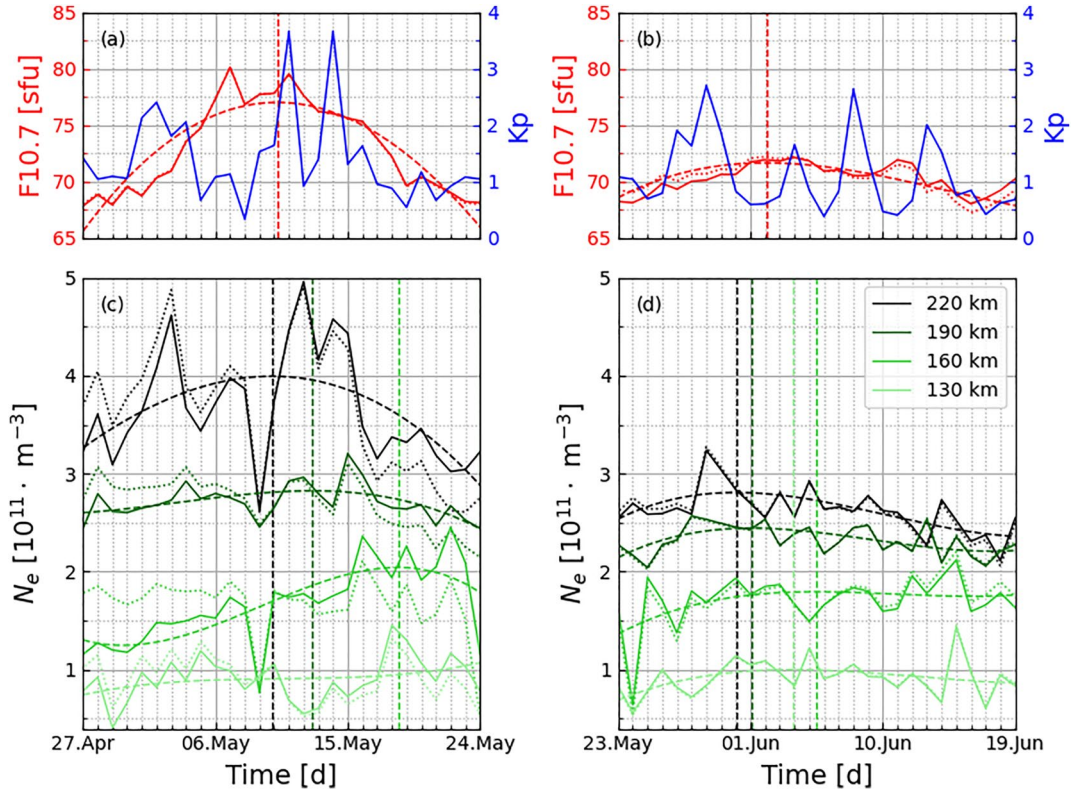

Figure 2. Solar radio flux index F10.7, Kp index, and electron density N_e for specific heights at the station Grahamstown (33.3°S and 26.5°E) from 27 April 2019 to 24 May 2019 (a, c) and from 23 May 2019 to 19 June 2019 (b, d). The electron density is selected at 130 km (light green), 160 km (green), 190 km (dark green), and 220 km (black). The dotted lines represent the data having their linear component compensated. The dashed lines represent a basis spline interpolation of each time series and the respective maximum of that interpolation (vertical line).

ionization and recombination processes. At lower heights, these processes have a less significant impact and different correlations and delays are observed. The N_e decrease (~30%) between the first and the second 27-day solar rotation period due to the solar activity decrease (~8%) influences the results of the delay estimation as well.

The comparison of the calculated delays in Figure 2 with the results based on TEC data at a different location by Schmölter et al. (2021) is difficult due to the different nature of the applied data sets. In addition, the interaction of solar and geomagnetic activity may affect the ionospheric state differently at two locations that, despite being selected in the same region, are not in close proximity. Nevertheless, the height-dependent analysis in Figure 2c shows that especially the first period is of interest for further investigation, since an impact of both, solar and geomagnetic activity, is observed at the N_e profile peak. For this reason, the analysis is extended and shown in more detail with the results in Figure 3 covering all available heights. In addition to the delay between F10.7 and N_e (see Figure 3b), the correlations of N_e with F10.7 and Kp are also shown (see Figure 3a). The correlation of Kp and N_e has a maximum of ~0.63 at 280 km and decreases at lower heights. At 220 km, the correlation is ~0.45 and then decreases strongly at lower heights. The profile of the correlation shows no significant peaks and therefore a continuous decrease of geomagnetic activity impact with height is observed. The correlation of F10.7 and N_e has its maximum of ~0.62 at 240 km. This height is above the maximum of the N_e profile (see Figure 1c) and is a peak in the correlation, that is otherwise constant from 190 to 270 km with a value of ~0.50. Below 190 km and above 270 km, the correlation decreases strongly.

Both, the correlation of N_e with F10.7 and Kp, vary strongly below 180 km indicating that the ionospheric state at these heights is controlled by processes that are either independent of solar and geomagnetic activity or impacted by complex interactions. Especially, forcing of the ionosphere from below due to various waves may contribute to the observed behavior (Laštovička, 2006; Vincent, 2015). From 180 to 240 km, the correlation of N_e with F10.7 is

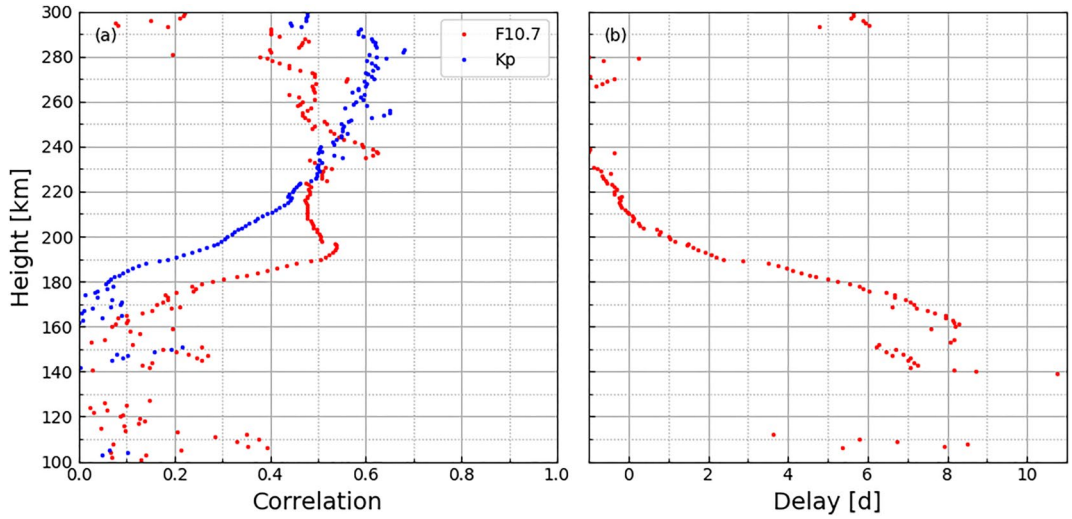

Figure 3. Correlation coefficients (a) of solar radio flux index F10.7 (red dots), Kp index (blue dots), and electron density N_e as well as delays (b) between F10.7 and N_e at the station Grahamstown (33.3°S and 26.5°E) from 27 April 2019 to 24 May 2019.

greater than with Kp due to the stronger increase starting at 180 km. Thus, the peak of the N_e profile is controlled by the solar variability, but then at increasing heights the geomagnetic activity has a stronger impact.

Due to weak correlation, delays at low heights cannot be inferred and only delays at heights from 190 to 270 km are further analyzed. Generally, the delay decreases with height from a maximum of 2 days at 190 km to an immediate ionospheric response above 230 km. On the one hand, this reflects the dominant correlation with Kp at these heights (changes in the ionospheric state due to short-term variations), but on the other hand, this also indicates that no accumulation processes occur (e.g., due to photodissociation at low altitudes). At heights below 230 km, which also cover the peak of the N_e profile, a delayed ionospheric response is observed since ionization and recombination processes due to solar activity are dominant and accumulation due to an imbalance of these processes can occur. While ionization due to O occurs almost immediately, recombination due to O_2 and N_2 is a slower process and the imbalance of these processes then leads to accumulation and the resulting delay (Ren et al., 2018; Schmölter, Berdermann, Jacobi, & Jakowski, 2020; Schmölter, Berdermann, Jakowski, & Jacobi, 2020).

Above 260 km, the ionospheric response indicates increasing delays which may be attributed to decreasing N_e (due to decreasing O^+) above the peak of the plasma density profile and propagation of the 27-day signature due to diffusion or transport processes (Vaishnav et al., 2021). From 160 to 190 km, the delay increases strongly (see Figure 3b) and weak correlations between N_e and F10.7 (see Figure 3a) are observed. However, at these heights, the weak correlation is due to the delay of several days and the solar 27-day signature are still present (see Figure 2c). This increase (strong shift of the 27-day signature) could be due to different processes. At these heights, the composition of the ionospheric plasma changes and NO^+, N_2^+, as well as O_2^+ contribute to the N_e profile due to different ionization and dissociation processes (Kelley, 2009). Transport processes and diffusion are expected to have an influence as well. Finally, forcing from below might contribute to the change of the delay as well (Laštovička, 2006; Vincent, 2015). The time series in Figures 2c and 2d indicate that during stronger solar activity the changes due to the 27-day solar rotation period can propagate further downwards and dominate the impact of the mentioned processes. Nevertheless, the delays of several days can only be explained with processes on longer time scales that do not occur at the peak of the N_e profile.

The observed delay is comparable to previous studies based on TEC and foF2 data (Schmölter, Berdermann, Jacobi, & Jakowski, 2020; Schmölter, Berdermann, Jakowski, & Jacobi, 2020) indicating that this region with the major contribution to the N_e profile also defines the overall response. The longer delays at other heights have a minor impact on the overall response, e.g., variations of the delay observed with TEC data (Schmölter, Berdermann, Jacobi, & Jakowski, 2020; Schmölter, Berdermann, Jakowski, & Jacobi, 2020). However, this is only indicated by the present results, as the weak correlations prevent a quantitative comparison. A different ionospheric

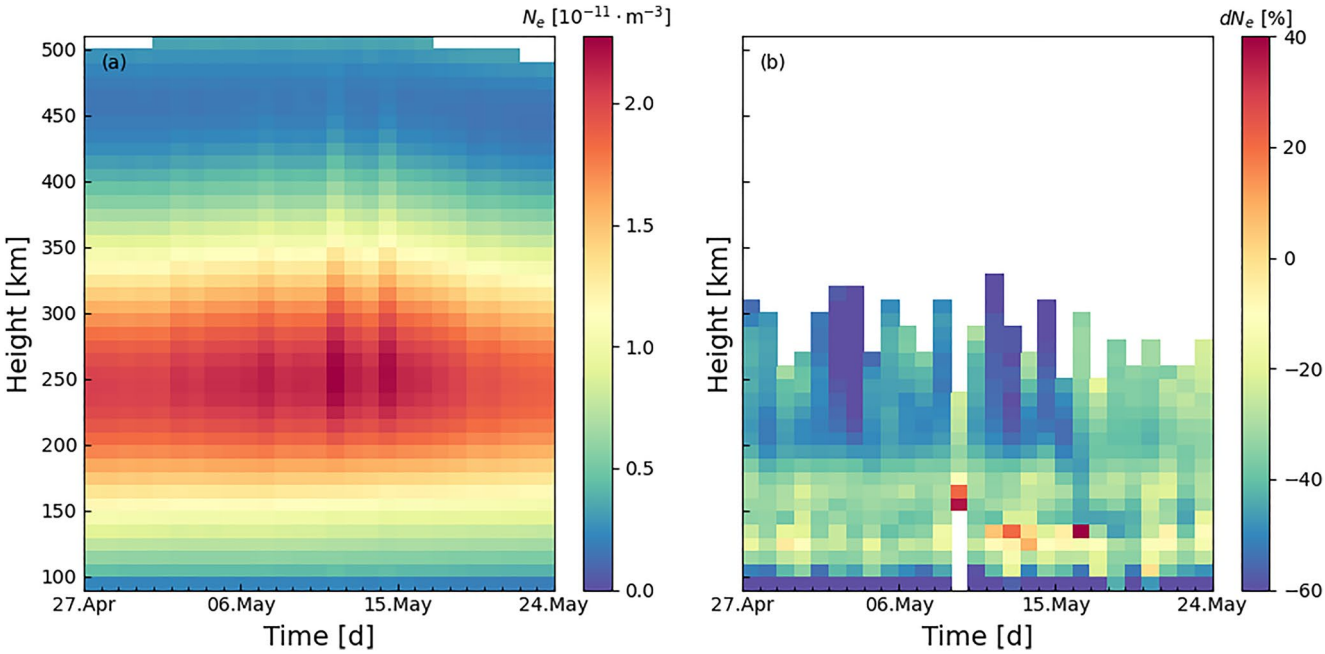

Figure 4. Modeled electron density N_e profile at grid point (33.75°S and 27.5°E) near station Grahamstown (a) and difference to observational data (b) from 27 April 2019 to 24 May 2019. Each bin represents the daily mean for a 10-km height level.

response in each of the two well-defined 27-day solar rotation periods from 27 April 2019 to 24 May 2019 and from 23 May 2019 to 19 June 2019 is confirmed with the N_e profiles in Figures 2 and 3.

4. Simulation of the Height-Dependent Delayed Ionospheric Response

The analysis of the ionosonde data is the entry point for further analysis of the selected time period using TIE-GCM simulations. First, a run with real conditions will be presented. Then, two model runs with artificial inputs for the 27-day solar rotation will be compared to investigate the underlying processes that define the height-dependent profile of the delay. Most of the analysis will be based on the electron density N_e, O^+ density n_{O^+}, O_2^+ density $n_{O_2^+}$, O mixing ratio Ψ_O, and O_2 mixing ratio Ψ_{O_2}.

4.1. Modeling of the 27-Day Solar Rotation Period From 27 April to 24 May 2019

For comparison with the observational results (see Figure 1), a TIE-GCM v2.0 model run in the 2.5° × 2.5° configuration is calculated. In order to converge to stable initial condition, the model runs for 30 days prior to the final simulation starting at 28 March 2019. This initial run is configured with default parameters. The final run from 27 April 2019 to 24 May 2019 uses the default configuration of TIE-GCM with the Heelis Electric Convection Field Model (Heelis et al., 1982) as the high-latitude potential model. The input forcing is used from the NASA/GSFC's OMNI data set.

Figure 4 shows the modeled N_e profiles in the same configuration as the measured data (daily mean for 10-km height level) in Figure 1. Changes due to the 27-day solar rotation period are well represented with the model results. The calculated N_e increases toward the maximum of the 27-day solar rotation period (strongly at the N_e peak) and the height of the N_e peak increases as well. During 7 May 2019, a pronounced N_e increase is observed, which is due to the corresponding increase of solar activity during that period (see Figure 1a). This variation, which is also observed with the ionosonde data (see Figure 1b), is thus well represented with the model results. Further significant N_e increases during 11 May 2019 and 14 May 2019 are due to the influence of geomagnetic activity during those days (see Figure 1a). Thus, these variations are also simulated as observed with the ionosonde data. The difference (see Figure 4b) shows that modeled N_e values are smaller than the measured

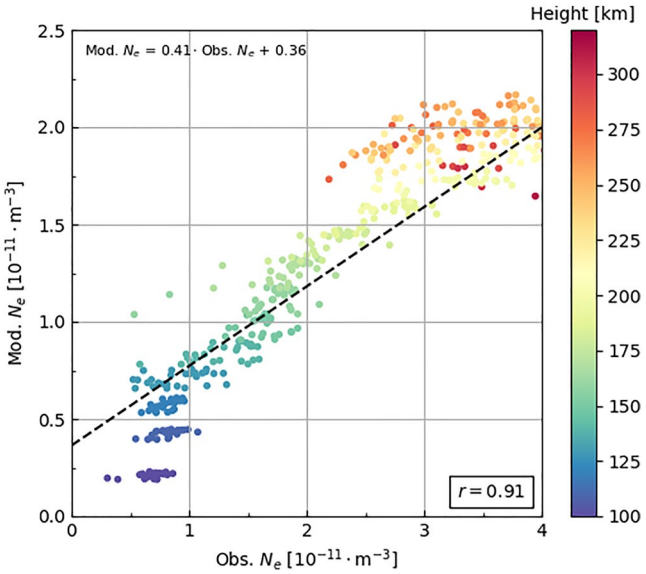

Figure 5. Scatter plot of the observed and modeled N_e profiles from 27 April 2019 to 24 May 2019. The height of each data point is given according to the colorbar. Correlation coefficient r, trend line (black dashed line), and corresponding parametrization are annotated in the plot.

values (~40%), but significant underestimation only occurs during periods of increased geomagnetic activity. Moreover, only heights above 200 km are affected. During other times and thus during dominant control by solar activity, the differences are smaller. The strong difference below 100 km may be attributed variations due to processes in the lower atmosphere which are not taken into account. For example, features of day-to-day variability during solar minimum conditions or during nighttime are not well represented by TIE-GCM, which is likely due to missing variations of perturbations from the lower atmosphere (Zhou et al., 2021). The quality of the ionosonde data must also be considered for the discussion of the observed differences, because uncertainties in the N_e profiles are to be expected despite the consideration of only data with AQI of 2 and 3. An additional comparison of model results from Figure 4 and measured values from Figure 1 is illustrated with the scatter plot in Figure 5. Model results and observations are excellently correlated ($r = 0.91$) with an absolute difference of ~40%. Stronger deviations are observed at heights above 200 km, which is due to the discussed influence of geomagnetic activity (see Figure 4b). The modeled N_e below heights of 110 km (heights converging toward the lower boundary of the model) is separated at two levels and is less correlated with the observed N_e (see also the corresponding difference in Figure 4b).

The good correlation of the model with the observations is affected during periods of increased geomagnetic activity, but the correlation with solar activity is well represented. For this reason, a more detailed height-dependent analysis of the delayed ionospheric response will also be simulated using TIE-GCM runs with artificial inputs (no influence of geomagnetic activity and sinusoidal 27-day solar rotation). Before that, however, the modeled N_e profiles from 27 April 2019 to 24 May 2019 are also discussed in more detail. The N_e profiles are characterized by composition of the neutral components and ionospheric plasma, as well as the various physical and chemical processes at the different heights. The good correlation for the N_e peak allows to investigate the influence of ionization and recombination related to O, while the excellent correlation for lower heights allows to study the role of photodissociation related to O_2 and transport processes. These are the processes of interest to characterize the delayed ionospheric response (Jakowski et al., 1991, 2002; Ren et al., 2018, 2019, 2020; Vaishnav et al., 2018, 2019).

The temporal variations of selected plasma components including electron density N_e, O^+ density n_{O^+}, and O_2^+ density $n_{O_2^+}$ are shown in Figure 6. The maximum at each height is marked with an upwards arrow and the distance to the maximum of the 27-day solar rotation period (the dashed line) defines the height-dependent delays. The delays of N_e and n_{O^+} at heights above 210 km are controlled by both solar and geomagnetic activity. The maxima at these heights are during the day of increased geomagnetic activity closest to the maximum of the 27-day solar rotation period (11 May 2019). A similar behavior is observed at heights from 170 to 210 km, but the maxima are during 7 May 2019. An even stronger shift of the maxima occurs at lower heights. The strong negative delays indicate a strong shift of the 27-day signature, which is also observed (albeit inversely) with the ionosonde data (see Figure 3b). This is caused in particular by more dominant $n_{O_2^+}$ at heights below 200 km, which is reduced throughout the whole period. In contrast to the observed difference, if an increase in $n_{O_2^+}$ would be modeled in the second phase of the 27-day solar rotation period, then a strong positive shift would be observed. Thus, the apparently large difference between model and observations depends on rather small variations. The immediate response at heights above 200 km is well represented.

At heights above 200 km, the accumulation of O^+ is observed due to increased ionization. This accumulation causes decreased recombination to O_2 at lower altitudes, and thus $n_{O_2^+}$ also decreases. This relation is already known from previous studies (Ren et al., 2018), but the results in Figure 6 show that the height-dependent analysis is strongly affected by O and O_2 variability. This is especially important to consider for studies that calculate the delayed ionospheric response using measurements integrated over height (e.g., TEC).

The described processes are also reflected by the neutral components. Figure 7 shows the O mixing ratio Ψ_O, O_2 mixing ratio Ψ_{O_2}, and N_2 mixing ratio Ψ_{N_2} with downward arrows marking the minimum at each height. The

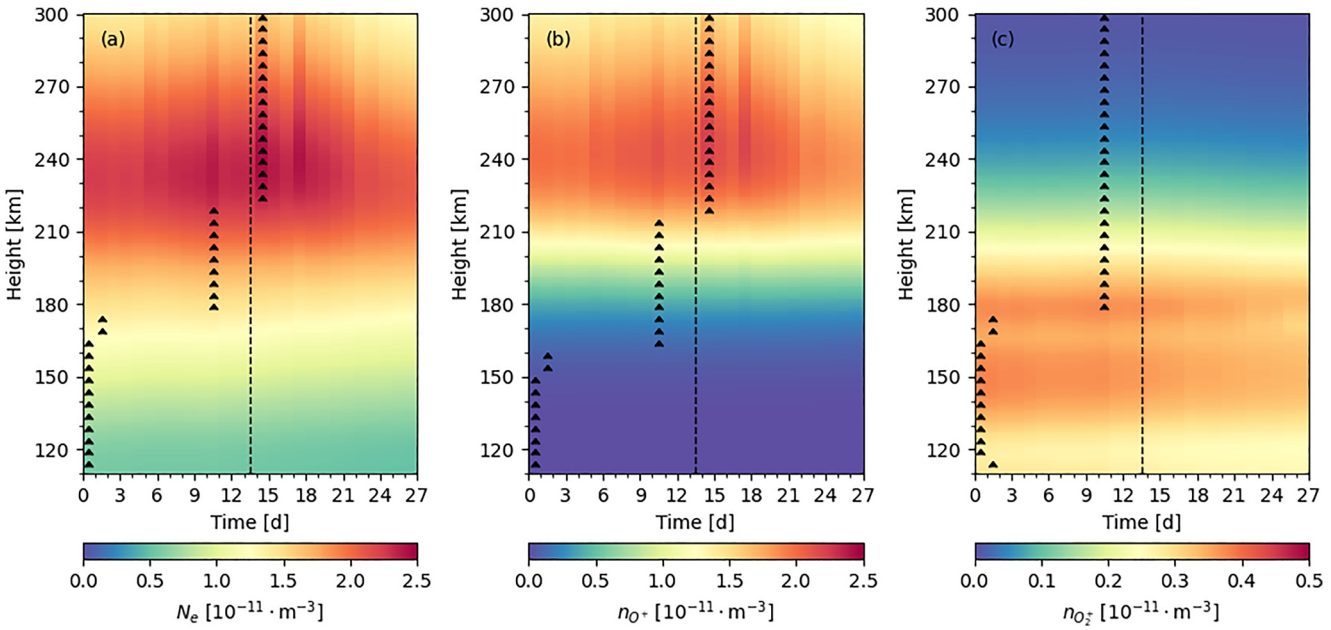

Figure 6. Progression of the modeled daytime N_e (a), n_{O^+} (b), and $n_{O_2^+}$ (c) profiles from 27 April 2019 to 24 May 2019. The upward arrows mark the maximum at each height (5-km grid) and the dashed vertical line marks the maximum of the 27-day solar rotation period. The corresponding delays (positive and negative) are thus given by the distance of the arrows from the dashed line.

variability of the neutral components is not affected by geomagnetic activity to the same extent as the ionized components. On the other hand, the correlation with solar activity (ionization and recombination processes) is more pronounced. The decrease of Ψ_O shows a minimum in the first half of the 27-day solar rotation period and an increase during the second half (see Figure 7a). This is consistent with the accumulation of O^+ at heights above 210 km. Ψ_{O_2} is decreased due to this accumulation and only recovers during the second half of the 27-day solar rotation period. Thus, recombination (O_2, but also N_2) was not strong enough to effectively counteract ionization

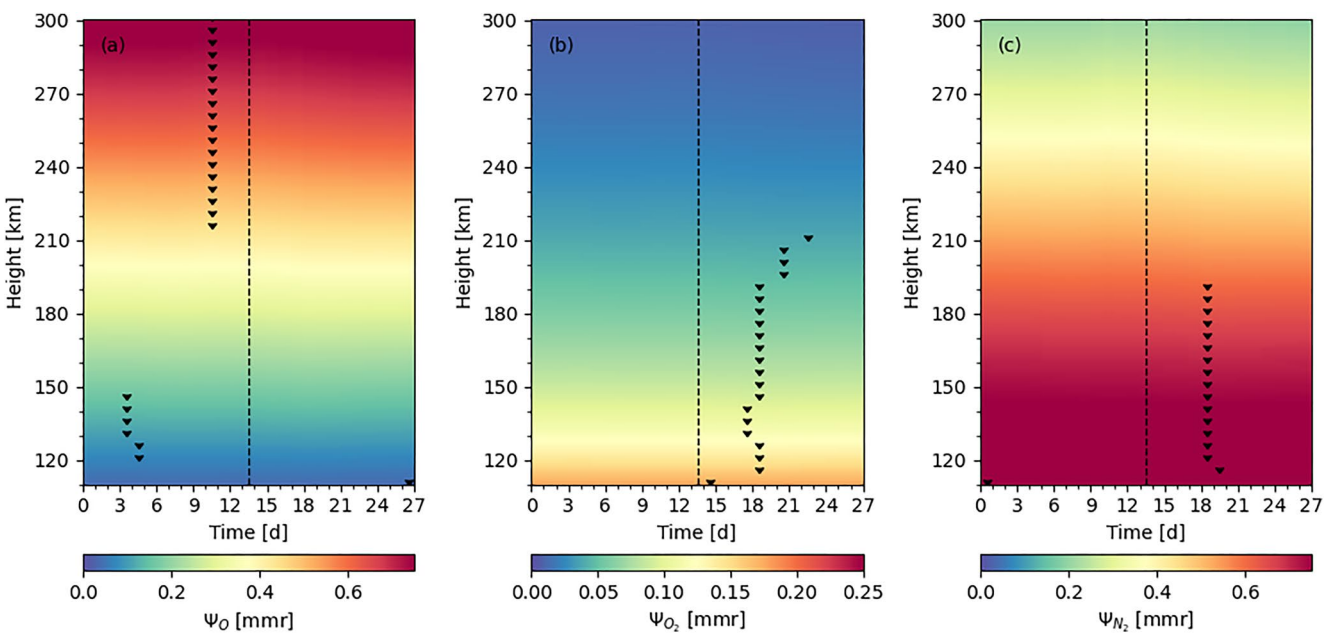

Figure 7. Progression of the modeled daytime Ψ_O (a), Ψ_{O_2} (b), and Ψ_{N_2} (c) profiles from 27 April 2019 to 24 May 2019. The downward arrows mark the minimum at each height (5-km grid) and the dashed vertical line marks the maximum of the 27-day solar rotation period. The corresponding delays (positive and negative) are thus given by the distance of the arrows from the dashed line.

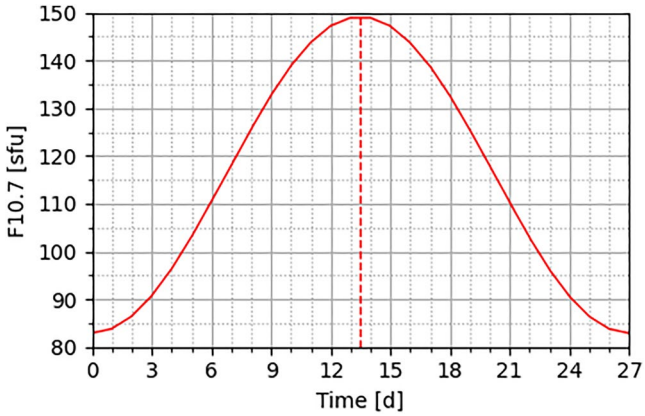

Figure 8. Artificial F10.7 input for the Thermosphere-Ionosphere-Electrodynamics General Circulation Model (TIE-GCM) model runs is shown with the red line and the maximum is marked with the red dashed line. The 81-day average of F10.7 is set to 118.40 sfu, which is approximately equal to the mean in the analyzed 27-day period.

and accumulation (O^+) until the observed minimum of O_2. In this context, photodissociation and transport processes have to be considered, since they affect the ionospheric composition as well. For this reason, these processes are discussed in more detail using further simulations in Section 4.2.

The delays of the N_e profile in Figure 6a, which describes the interaction of all ionized parts, are defined by n_{O^+} and $n_{O_2^+}$ at the different heights. Thus, at heights above 220 km delays of ~1 day occur (dominated by O^+) and below 220 km a significant change of the delay (phase shift of the 27-day solar rotation period) is observed. This result is partially in good agreement with the observations in Figure 3b showing increasing delays above 200 km and a mostly immediate response to solar activity changes. However, the delay changes below 200 km are opposite. This could be due to differences in the modeling and the actual processes or due to the methods used in this study (e.g., impact of the applied interpolations). In any case, significant phase shifts of the 27-day solar rotation period occur for the lower heights. While the delay is driven by the direct ionization and recombination processes at the respective heights, the interaction of the plasma and neutrals above and below 200 km is crucial as well. The recombination of O^+ at low heights creates O_2 which contributes then to the O^+ accumulation at greater heights via photodissociation. Both processes are also directly related to diffusion and other transport processes, which create the necessary mixing of the components allowing the chemical processes to occur. In conclusion, TIE-GCM seems to produce a reasonable representation of the processes of interest and can be applied to understand their respective influences. Based on the presented results, further model runs can be performed to investigate the different processes using simplified inputs for the 27-day solar rotation period. In particular, the influence of geomagnetic activity is eliminated in the following simulations in order to more accurately describe the variations due to solar activity.

4.2. Modeling of an Artificial 27-Day Solar Rotation Period

The artificial runs use the TIE-GCM v2.0 model in its 2.5° × 2.5° configuration as the real condition model run. In order to converge to stable initial condition, the TIE-GCM runs for 30 days prior to the final simulation starting at 21 September 2010. This initial run was configured with default parameters. Both model runs start at 21 October 2010 and are calculated with default parameters except for the switched off auroral parameterization as well as the switched off high-latitude potential model. The influence of noise in solar activity is reduced by applying an artificial noise free sinusoidal time series for the F10.7 input as shown in Figure 8.

N_e profiles at a midlatitude location are selected for the analysis. A significant response to solar activity occurs at 51.25°N, so this geographic latitude is well-suited. The geographic longitude is not important due to the configuration of the model run and is therefore arbitrarily set to 10°E. Thus, with the given period from 21 October to 18 November and the chosen location in the Northern Hemisphere, an autumn period is analyzed. Even though the model run is simplified, these conditions must be taken into account for composition changes and transport processes especially in the lower ionosphere (Chang et al., 2013; Qian et al., 2009). The analysis of a different location than in the previous model run is an intended change, since the following analysis focuses only on the interaction of the dominant processes. These can be more easily identified with the chosen setup. Otherwise, adjusting the solar activity until the features appear for a specific location would be a time-consuming procedure without any benefits.

The variations of N_e, n_{O^+}, and $n_{O_2^+}$ are shown in Figure 9. Compared to the variations in Figure 6, the absolute values are larger and the height of the N_e peak (at ~270 km) is also higher. The height-dependent variations of N_e are again controlled by the respective contributions of n_{O^+} and $n_{O_2^+}$ and at the end of the period, the ionospheric plasma is approximately back to the initial state. The n_{O^+} profile in Figure 9b shows positive delays at all heights excluding the range from 180 to 200 km. At these heights (transition from O^+ to O_2^+ peak), a continuous increase of n_{O^+} is observed indicating a strong accumulation of O^+ in this region. The delay decreases from approximately 2 to 0 days at heights below 180 km. At heights above 210 km, the delay decreases from approximately 4 to 2 days. Thus, the right shift of the 27-day signature is observed for the whole n_{O^+} distribution. The $n_{O_2^+}$ profile in

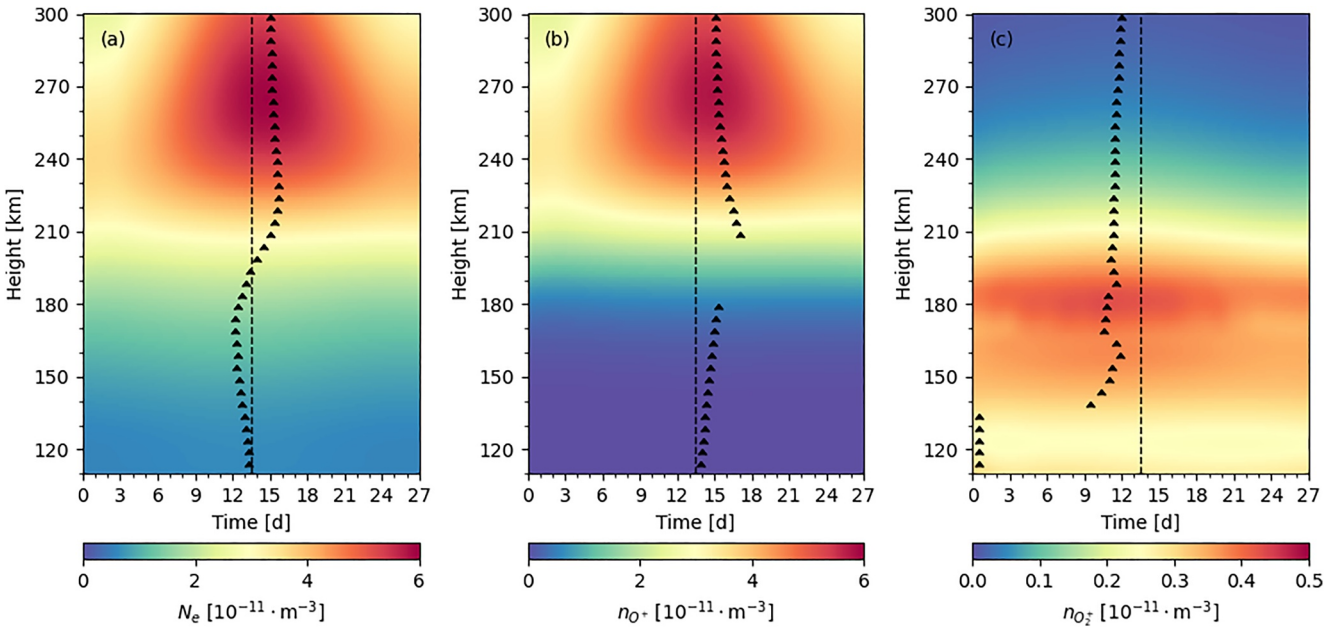

Figure 9. Progression of the modeled daytime N_e (a), n_{O^+} (b), and $n_{O_2^+}$ (c) profiles from 21 October to 18 November. The upward arrows mark the maximum at each height (5-km grid) and the dashed vertical line marks the maximum of the 27-day solar rotation period. The corresponding delays (positive and negative) are thus given by the distance of the arrows from the dashed line.

Figure 9c shows negative delays at all heights. The delay is ∼−2 days at 300 km and decreases with decreasing heights up to ∼−5 days. At 160 and 190 km, small increases of the delay occur which are related to increased $n_{O_2^+}$. At heights below 140 km, a strong shift of the 27-day signature is observed due to a continuous decrease of $n_{O_2^+}$ (similar behavior as in Figure 6c). The delay of the N_e profile in Figure 9a correlates at heights from 220 to 300 km with the delay of the n_{O^+} profile. At heights from 180 to 220 km, the delay decreases turning negative and at heights below 180 km, the delay increases up to 0 days again. Thus, the contribution of the $n_{O_2^+}$ profile is less pronounced and superimposed with the contribution of the n_{O^+} profile. The integrated N_e delay is 0.57 days, which can be further specified by taking into account the mean density distribution (applied as weights). The weighted delay of 0.70 days reflects the control of the N_e peak (increased delay), but also shows that the height-dependent plasma composition is important to consider if the delayed ionospheric response is estimated with integral measurements (e.g., TEC).

The transition region between n_{O^+} and $n_{O_2^+}$ peak is ∼80 km in Figure 9 compared to ∼50 km in Figure 6. Thus, a broader region is present in which the ionospheric plasma is defined by the mixing of both ionized species. This must be taken into account for the analysis of the delay with respect to transport processes and especially diffusion processes. While the role of processes such as eddy diffusion for the delayed ionospheric response have been extensively studied (Vaishnav et al., 2021), consideration of plasma distribution could improve the understanding of the complex interactions. Section 4.3 briefly discusses these topics based on the available results.

The occurring O^+ accumulation (and corresponding decrease of O_2^+) is also reflected by the Ψ_O and Ψ_{O_2} profiles in Figure 10. At heights below 180 km, Ψ_{O_2} decreases until the second phase of the 27-day solar rotation period. This decrease, which is related to the accumulation of O^+ at the N_e peak, also decreases the photodissociation rate of O_2 causing a continuous decrease of Ψ_O at these heights. At heights above 180 km, the minima of Ψ_O occur increasingly later due to the dominant role of ionization and recombination related to O. The strong shift of the 27-day signature for O and O_2 at low heights, which is also observed in Figure 7, reflects the role of ionization and recombination on the delayed ionospheric response (Ren et al., 2018) and reveals to which extent the photodissociation has to be considered. The Ψ_{N_2} profiles are estimated according to the implementation (Yu et al., 2021) as

$$\Psi_{N_2} = 1 - \Psi_{O_2} - \Psi_O, \tag{6}$$

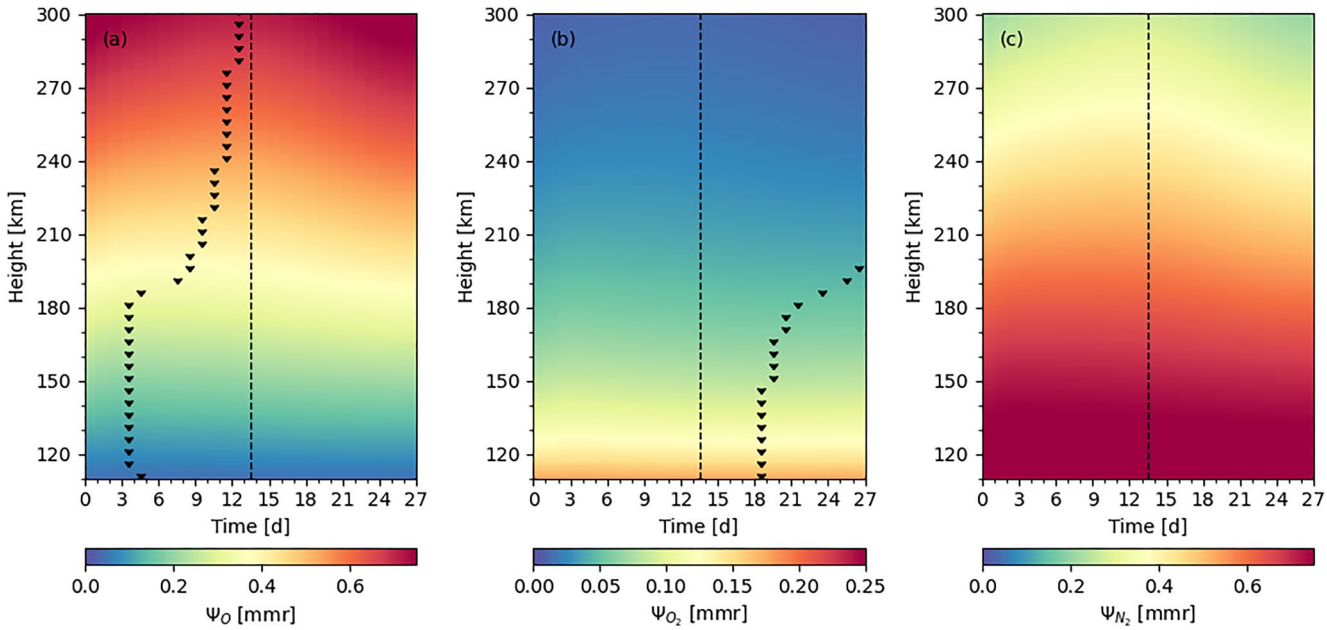

Figure 10. Progression of the modeled daytime Ψ_O (a), Ψ_{O_2} (b), and Ψ_{N_2} (c) profiles from 21 October to 18 November. The downward arrows mark the minimum at each height (5-km grid) and the dashed vertical line marks the maximum of the 27-day solar rotation period. The corresponding delays (positive and negative) are thus given by the distance of the arrows from the dashed line.

and present the interaction of O and O_2. For that reason, the results are shown in Figures 7 and 10 to provide a complete overview of the major species.

The variation of n_{O^+} is also in good agreement with the results by Vaishnav et al. (2021). That study includes an analysis of the delay height profile for the O^+ density using results from Coupled Thermosphere Ionosphere Plasmasphere Electrodynamics Model (CTIPe) runs. The calculated delay by Vaishnav et al. (2021) decreases from the O^+ density maximum with decreasing height, but converges to a constant value at ∼180 km. At this height, the O^+ density then directly follows the solar activity. The accumulation of an ionized species and thus the presence of a corresponding delayed response is always strongly related to the neutral composition, and depending on the width of the ionospheric height profile, abrupt, or smooth transition regions between layers of different compositions occur (see Figures 6b and 9b). Self-explanatory, the delayed N_e and overall ionospheric response (e.g., TEC) are a product of the different components. This difference was also shown by Schmölter, Berdermann, Jacobi, & Jakowski, 2020; Schmölter, Berdermann, Jakowski, & Jacobi, 2020 with F2 layer specific parameters from ionosonde data and vertical TEC.

4.3. Contribution of Transport Processes to the Delayed Ionospheric Response

Vaishnav et al. (2021) primarily investigated the role of the eddy diffusion on the delayed ionospheric response via the ratio of O and N_2 observing more immediate changes for increased eddy diffusion. The results suggest that increased eddy diffusion causes faster transport processes, which in turn increases the mixing of different species and leads to increased loss rates (Vaishnav et al., 2021). This change decreases and stops the accumulation of ionized parts and therefore a smaller or no delay occurs. The transport processes (especially concerning the neutral parts) can further be impacted by temperature and pressure changes (Rishbeth, 1998). Ren et al. (2020) investigated with TIE-GCM the different peak response times to the 27-day solar rotation period for thermospheric mass density of O and N_2 as well as neutral temperature. The results of that study indicate that the response of both neutral species is defined by the counteracting of barometric processes and the change of the abundance of the species (Ren et al., 2020). The response of both neutral species is further affected by the meridional circulation of the thermosphere causing latitudinal structures (Ren et al., 2020).

The variations of the various neutral and ionized species in Figures 6, 7, 9, and 10 are shown against the heights and thus include the changes of the pressure levels. This representation was chosen on the one hand to provide a

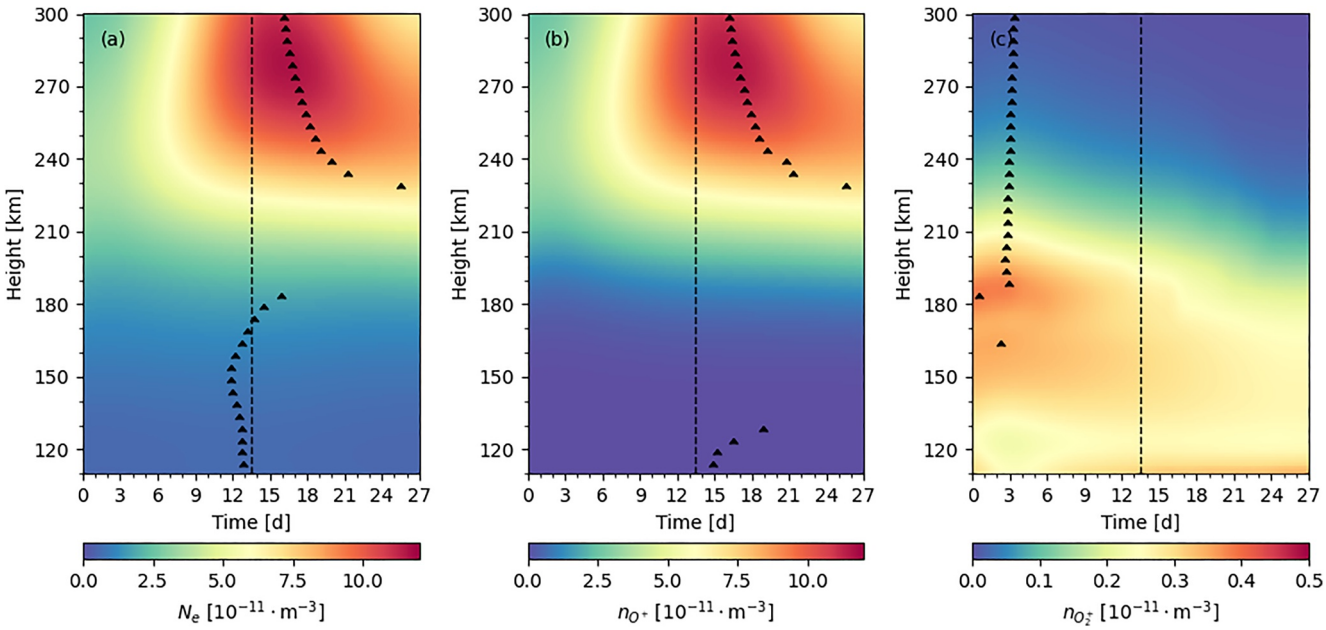

Figure 11. Progression of the modeled daytime N_e (a), n_{O^+} (b), and $n_{O_2^+}$ (c) profiles from 21 October to 18 November. The upward arrows mark the maximum at each height (5-km grid) and the dashed vertical line marks the maximum of the 27-day solar rotation period. The corresponding delays (positive and negative) are thus given by the distance of the arrows from the dashed line. The eddy diffusion is set to have no significant impact in this model run.

better comparability to the observations and on the other hand to consider all contributions to the observed delay. The height changes of the pressure levels due to the changes of the neutral temperature in response to the 27-day solar rotation period do not by themselves affect the composition of the different species (Rishbeth, 1998). Nevertheless, these changes have their own contribution to the delay (Ren et al., 2020). Added to this are the transport processes at the various pressure levels (according to the thermodynamic equation for neutral parts or more specifically the O^+ transport equation). Thus, e.g., horizontal winds, vertical winds, and ambipolar diffusion (eddy and molecular diffusion) are implemented.

This study can confirm the identified role of the eddy diffusion according to analysis using CTIPe simulations by Vaishnav et al. (2021) with TIE-GCM simulations. Performing the model run of the artificial 27-day solar rotation period with eddy diffusion K_E set to a negligible value ($K_E \rightarrow 0$) shows n_{O^+} changes that are as expected (see Figure 11). The observed delays are longer at the N_e and n_{O^+} peak, and at heights from 210 to 230 km, the accumulation of O^+ is stable causing the delays to extend beyond the second half of the 27-day solar rotation period. It must be considered that the ambipolar diffusion K, which is used in the O^+ transport equation, also includes the molecular diffusion D_A according to

$$K = D_A + K_E, \tag{7}$$

but nonetheless the major interference in the dynamic processes, shows the crucial role of transport for the loss of O^+ and the delayed ionospheric response. $n_{O_2^+}$ decreases continuously for the entire 27-day solar rotation period, which is also due to the accumulation of O^+ (decreased loss). Under realistic conditions, variations of the eddy diffusion are smaller (Salinas et al., 2016; Wu et al., 2017) and therefore a smaller influence on the delay is expected. The effect on the neutral components must also be considered when variations in eddy diffusion occur (Qian et al., 2009, 2013). However, this is not the scope of this study.

Figure 12 shows the daily mean neutral vertical wind $\overline{W}$, nighttime neutral vertical wind $W_\downarrow$ (from 21:00 to 03:00 LT) and daytime neutral vertical wind $W_\uparrow$ (from 9:00 to 15:00 LT) corresponding to the results of the first of the artificial 27-day solar rotation period (see Figures 9 and 10).

$W_\downarrow$ as well as $W_\uparrow$ follow the solar activity, but the observed delays are varying for different heights. Above 210 km, the delay for both parameters is negative (1–3 days) and thus is ahead of the N_e and n_{O^+} changes (see Figures 9a and 9b). There is a good agreement with the delay observed for $n_{O_2^+}$ (see Figure 9c). Below 210 km, $W_\downarrow$ follows

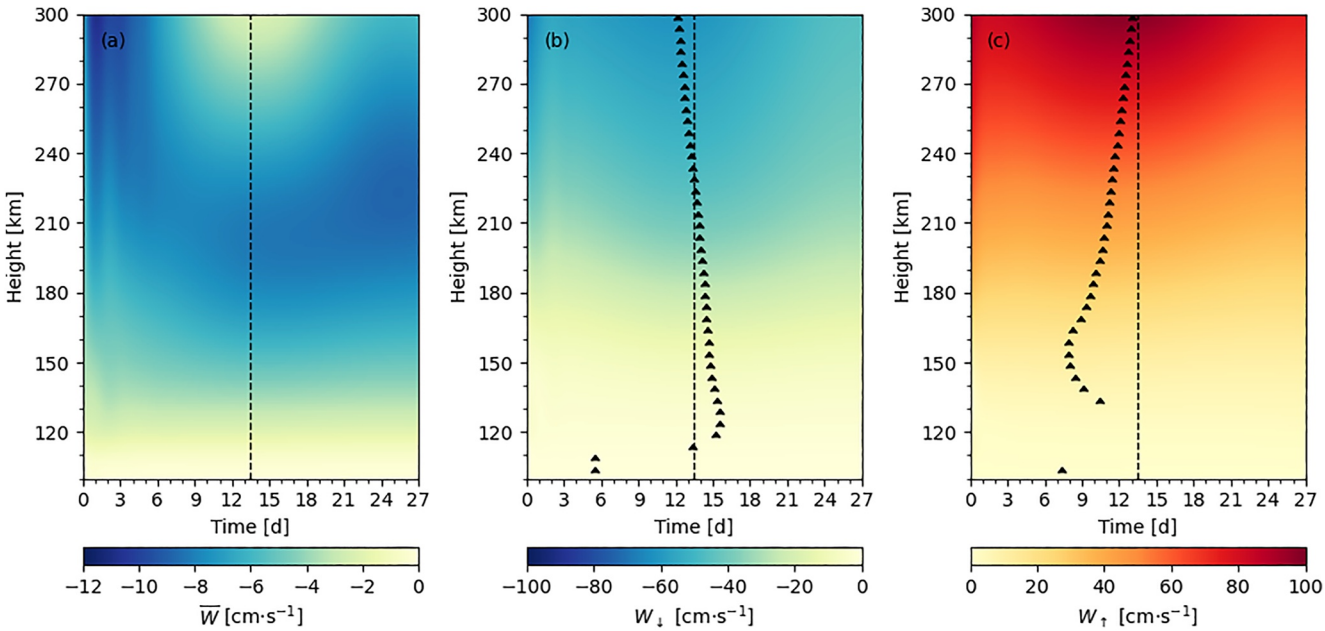

Figure 12. Daily mean neutral vertical wind $\overline{W}$ (a), nighttime neutral vertical wind $W_\downarrow$ (b), and daytime neutral vertical wind $W_\uparrow$ (c) profiles from 21 October to 18 November. The downward arrows (b) mark the minimum at each height (5-km grid), the upward arrows (c) mark the maximum at each height (5-km grid) and the dashed vertical line marks the maximum of the 27-day solar rotation period.

the solar activity and no significant delay occurs. $W_\downarrow$, on the other hand, has longer delays down to a height of 150 km. A strong phase shift occurs for $W_\uparrow$ at these heights compared to the 27-day solar rotation. This behavior is similar to the results of Ψ_{O_2}. Overall, W changes especially at height from 180 to 240 km with a continuous decrease of upward winds, resulting in downward winds dominating this region significantly during the second half of the 27-day solar rotation period. This downward transport counteracts the O^+ accumulation at the beginning of this phase and favors recombination at lower heights. This may explain how the ionospheric plasma (see Figure 9) can return to its initial state despite the observed delays. Future work could explore this reasoning with observations, e.g., neutral wind profiles in line of sight measured by the NASA Ionospheric Connection Explorer (ICON) covering the discussed height region (Harding et al., 2017; Maute, 2017).

5. Discussion

The analysis has provided a first insight into the height profile of the delay using TIE-GCM simulations. Several parameters have not yet been taken into account and the comparison to observations has only been performed for one case study. Thus, the analysis of delay can be extended in two aspects in future studies. The dependence on other parameters (e.g., wavelength of the solar EUV radiation) can be taken into account and the comparison to observations can be performed using statistical methods for a large number of 27-day solar rotation periods (e.g., SEA). The necessity of these methods is briefly discussed here.

5.1. Height-Dependent and Wavelength-Dependent Absorption of Solar EUV

The ionization rates I of major species are calculated by TIE-GCM as a function of heights Z and wavelengths λ according to the Beer-Lambert law

$$I(\lambda, Z) = I(\lambda, \infty) \cdot e^{-\tau(\lambda, Z)}. \tag{8}$$

The optical depth τ introduces the dependence on height and wavelength by considering the column densities N for each species j and the respective total absorption cross-section σ according to

$$\tau(\lambda, Z) = \sum_j \sigma_j(\lambda) \cdot N_j(Z) \cdot Ch. \tag{9}$$

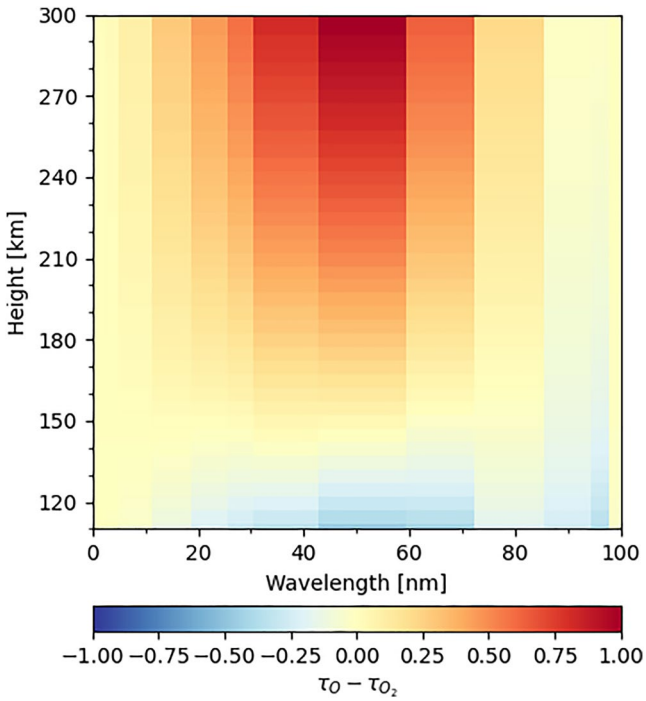

Figure 13. Difference of the optical depth τ of O and O_2 at 26 October. The optical depths are in favor of O for positive values and in favor of O_2 for negative values. The difference is normalized.

With these equations and the executed model runs, τ can be calculated for O and O_2 to estimate the respective part of the occurring absorption. Since a qualitative description is sufficient for the comparison intended here, the Chapman grazing incidence integral correction factor Ch is estimated according to

$$Ch = \sec\chi \text{ with } \chi < 60^\circ \tag{10}$$

and the solar zenith angle χ is set to a single value. Figure 13 shows the calculated τ_O and τ_{O_2} as a normalized difference. The height and wavelength regions dominated by τ_O are defined by ion production of $O^+(^4S)$, $O^+(^2D^0)$, and $O^+(^2P^0)$, but overall the distribution appear as one region with a maximum at 54 nm and an increase in height. On the other hand, there are two major regions dominated by τ_{O_2}. Ion production of O_2^+ occurs over most of the EUV spectrum with two maxima at 54 and 97.5 nm. The photodissociation has a maximum at 102.7 nm and decreases with wavelength. Both regions can be distinguished from each other in Figure 13 and thus a more complex distribution than for τ_O is present. While for wavelengths from approximately 20 to 80 nm τ_O and τ_{O_2} compete (with a transition region around 150 km), in the wavelength range above 80 nm τ_{O_2} dominates for all heights. The distribution of τ_O and τ_{O_2} for the selected heights and wavelengths again shows how crucial the consideration of neutral parts and different processes is for the state of the ionospheric plasma and the delayed response to solar activity changes (see also Figures 9 and 10).

Therefore, in future studies, the dependence of wavelength should be considered and especially different conditions for wavelengths at approximately 60 and 100 nm should be investigated (impact of ionization and photodissociation). This is not possible with model runs that apply the F10.7 solar proxy and instead requires that measured solar EUV flux data are used. For example, changes may occur in some wavelengths of the EUV spectrum that do not correlate with F10.7 changes (Huang et al., 2016). Taking these changes into account could be crucial for long-term trend analysis of the delayed ionospheric response.

5.2. SEA of the F2 Layer

The SEA technique (also known as composite analysis) was used to extract a solar 27-day signature in foF2 and hmF2 time series determined from the Grahamstown ionosonde measurements. The analysis is based on all available data for the years from 2018 to 2020. The composite Mg II index provided by the university of Bremen (see Section 2.2) is used as the solar proxy for the SEA. The SEA has been described in detail in many other publications (e.g., Rong et al., 2020; von Savigny et al., 2019) and only a very brief summary is given here. In a first step anomaly time series of Mg II, foF2 and hmF2 are determined by subtracting a 35-day running mean from the original time series (see Figure 14). As Figure 14 illustrates, apparent solar 27-day signatures in foF2 and hmF2 are visible, particularly in the second half of 2019 and the second half of 2020. However, also during periods without pronounced 27-day cycles in the Mg II index similar variations are present, which may potentially be caused by planetary wave signatures from the lower atmosphere. Rong et al. (2020) and von Savigny et al. (2019) discussed these effects on quasi-27-day signatures in the stratosphere and mesosphere.

The calculated anomaly time series are then smoothed with a 5-day running mean in order to suppress day-to-day variability. In a following step, the so-called epochs are defined by automatically identifying the 27-day maxima of the Mg II index, which constitute the centers of the epochs used for further analysis. In order to allow for a more robust identification of a solar 27-day signature only periods with enhanced solar 27-day variability as indicated by the red circles in Figure 14 are used. The partial foF2 (or hmF2) data sets corresponding to the different epochs are written to the rows of a matrix and the main step of the SEA is to average the matrix column-wise. The basic idea is that atmospheric variability unrelated to the solar forcing cancels out by the averaging, while a potential 27-day solar signature in the analyzed time series is retained.

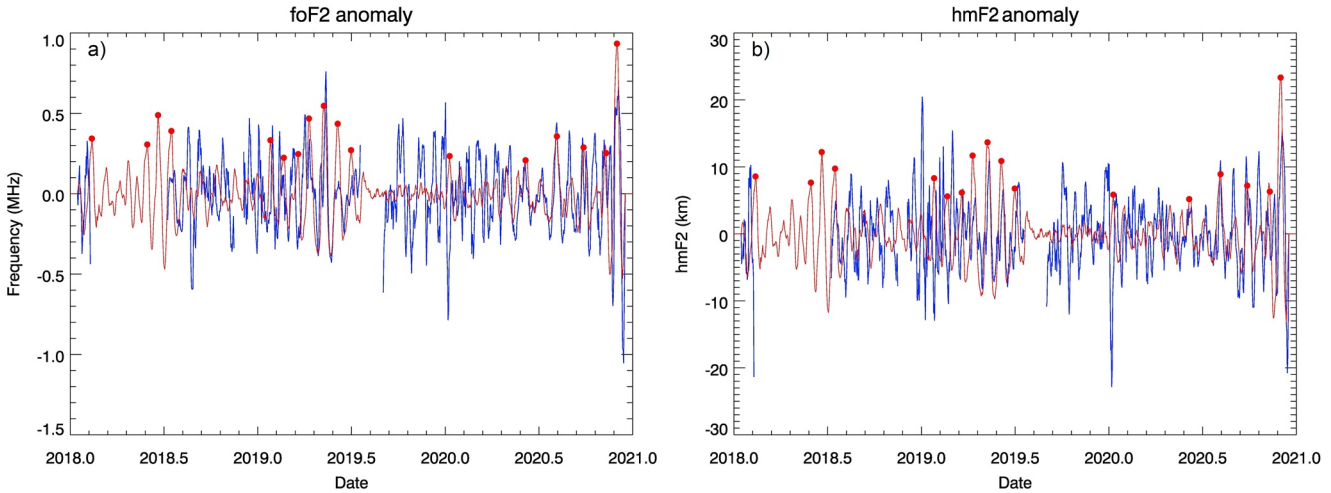

Figure 14. Anomaly time series of foF2 (a) and hmF2 (b) for the years from 2018 to 2020 in blue together with the Mg II index anomaly time series in red (and scaled by arbitrary factors). The identified Mg II index maxima (i.e., the epoch centers) are shown as red solid circles.

Figure 15 shows the results of the SEA applied to the Grahamstown foF2 and hmF2 time series. The red solid lines show the epoch-averaged Mg II index anomaly scaled with an arbitrary factor to make the anomaly visible. The blue solid lines correspond to the epoch-averaged foF2 (or hmF2) anomalies and the difference between the blue solid and dotted lines is the errors of the mean of the epoch-averaged anomaly values determined from the data values from all epochs analyzed. Apparently, the error of the mean is significantly smaller than the visible quasi-periodic variation in the epoch-averaged anomalies. This is already a clear indication that the identified signatures do not appear by chance.

In order to estimate the significance of the results, a Monte-Carlo approach as in von Savigny et al. (2019) is applied. In short, the test is based on repeating the SEA 1,000 times with randomly chosen epoch centers and fitting a 27-day sinusoidal function to the epoch-averaged anomaly of each random ensemble. Then the fraction of random ensembles associated with sinusoidal amplitudes exceeding the amplitude of the actual SEA is determined. The lower this fraction, the more likely a solar effect is present in the analyzed time series. This fraction is 0.4% for foF2 and 0.5% for hmF2, respectively. In other words, the identified 27-day solar signatures in foF2 and hmF2 have to be considered highly significant. Figure 16 shows as an example, the sinusoidal fits for the 1,000

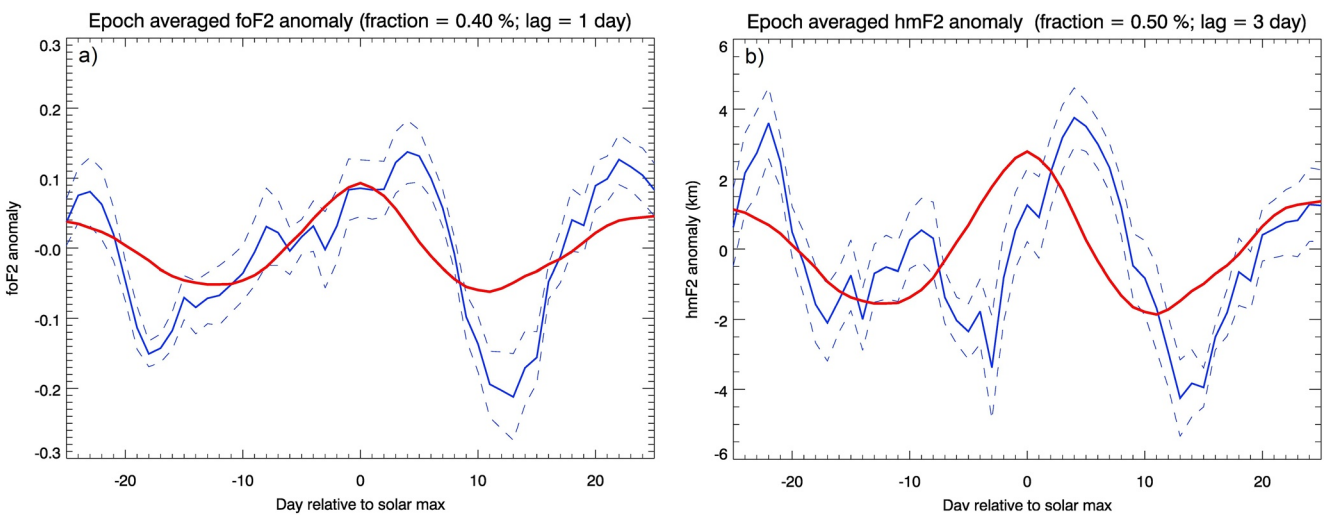

Figure 15. Superposed epoch analysis (SEA) results for foF2 (a) and hmF2 (b) as described in the text. The red solid lines show the epoch-averaged Mg II index anomaly (scaled by arbitrary factors). The blue solid lines correspond to the epoch-averaged anomalies of foF2 and hmF2, respectively. The time lags given in the panel titles are based on a cross-correlation between the Mg II and the foF2 (or hmF2) epoch-averaged anomalies.

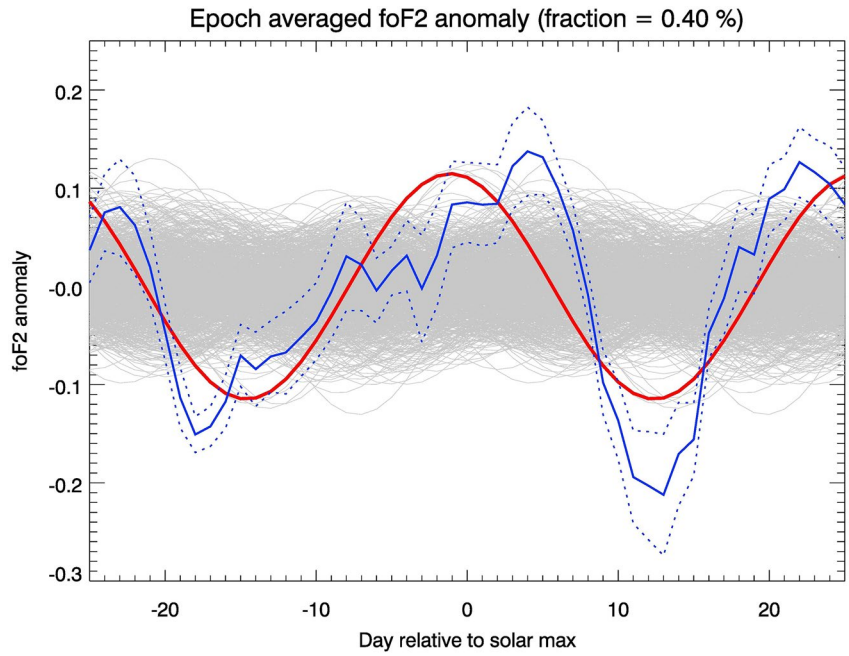

Figure 16. Sample result for the Monte-Carlo significance test for foF2. The red line is a sinusoidal fit to the epoch-averaged foF2 anomaly.

random ensembles for the foF2 analysis as gray lines, together with the results of the actual SEA. The red line is a sinusoidal fit to the epoch-averaged foF2 anomaly.

The SEA approach, which has been applied to F2 layer specific parameters, could be extended to N_e dependent on height or pressure level. However, this requires a much more extensive analysis due to the vertical variations of the N_e profile. For example, the SEA approach could be applied to large height ranges initially (e.g., 100 km) and then be progressively refined to investigate specific regions. Another approach could be the calculation based on relative heights above and below the N_e peak. Either way, this would require a much more extensive analysis, that future studies may implement.

5.3. Solar 27-Day Signatures in the Middle Atmosphere

Solar 27-day signatures have also been reported in several parameters or constituents in the middle atmosphere (i.e., stratosphere and mesosphere) including temperature (e.g., Dyrland & Sigernes, 2007; Hood, 1986; Rong et al., 2020; Thomas et al., 2015; von Savigny et al., 2012), ozone (e.g., Fioletov, 2009; Hood, 1986), odd hydrogen (Wang et al., 2015), mesospheric water vapor (Thomas et al., 2015), atomic oxygen in the MLT region (Lednyts'kyy et al., 2017), radio reflection heights (von Savigny et al., 2019), and even in noctilucent clouds (Robert et al., 2010)—also known as polar mesospheric clouds. In many cases, the identification of solar 27-day signatures in middle atmospheric parameters is relatively straightforward and typically based on correlation analyses or SEA. However, attributing the signatures to the exact physical and chemical drivers is usually very difficult.

One main difficulty lies in the separation of direct photochemical effects and dynamical effects. Dynamical effects may be triggered, e.g., by 27-day signatures in stratospheric/mesospheric temperature leading to thermal wind adjustments, followed by changes in the filtering of gravity waves. Theses processes are currently not well understood. In addition, there may be dynamical signatures with periods close to 27-day, which may be entirely unrelated to the solar forcing, e.g., the 28-day Rossby Wave (1,4) mode (Zhao et al., 2019).

An example of middle atmospheric solar 27-day signatures with particular importance also for the results presented in the current study, is the unexpected delay in the solar 27-day signature in tropical upper mesospheric atomic oxygen found by Lednyts'kyy et al. (2017). Lednyts'kyy et al. (2017) employed O I green line nightglow

emission measurements with SCIAMACHY on board ESA's Envisat spacecraft to retrieve O density profiles in the height range from 85 to 105 km. The analysis showed a statistically highly significant solar 27-day signature in O densities with a relative amplitude of about 1.5% and a delay relative to the solar forcing of about 13 days. One potential reason for this relatively long delay could be related to the transport time from the main O production region in the lower thermosphere down to MLT altitudes, where SCIAMACHY measurements are available.

The different responses to the 27-day solar rotation period could be investigated with mesospheric, thermospheric, and ionospheric measurements (e.g., GOLD O_2 density profiles, ICON O^+ density profiles, ionosonde N_e profiles, and SCIAMACHY O density) in the future. Such an analysis could either confirm a relation between the observed signatures or define boundaries for the impact of specific processes (e.g., O production and propagation due to transport processes). The complementary modeling could be realized using the Thermosphere-Ionosphere-Mesosphere Electrodynamic General Circulation Model (TIME-GCM), which extends the lower boundary of TIE-GCM to 30 km, or using the Whole Atmosphere Community Climate Model with thermosphere and ionosphere extension (WACCM-X). Methods for such an analysis (case or statistical studies) are introduced within the present study for both, observational and model data.

6. Conclusion

The analysis by Schmölter et al. (2021) for two 27-day solar rotations was extended in the present study using ionosonde profiles. With respect to the correlation, the delay was calculated for the available heights (see Figures 2 and 3) showing the following results:

1. The electron density N_e at heights above 200 km is correlated with both solar and weak geomagnetic activity. The correlation with geomagnetic activity increases with height. These results are in good agreement with the described thermospheric response during that period by Cai et al. (2021)
2. The ionospheric response to the solar activity at the N_e peak is immediate, but the delay increases with decreasing heights. However, the delays at low heights can only be analyzed to a limited extent, since the correlation with solar activity is not sufficient at these heights. Other processes dominate the ionospheric state at lower heights
3. The 27-day solar rotation period from 7 April 2019 to 24 May 2019 is well-suited for a comparison with TIE-GCM simulations due to the good data quality

The ionospheric changes, which were observed using the ionosonde data, were further simulated with TIE-GCM showing the following results:

1. Observed and modeled N_e are in good agreement (correlation coefficient of 0.91), but TIE-GCM underestimates the plasma density (see Figure 5). This difference can be attributed to the underestimated N_e in the topside ionosphere during days with enhanced geomagnetic activity and the lower boundary (see Figure 6b)
2. The modeled delayed ionospheric response is driven by solar and weak geomagnetic activity changes (see Figure 6). The general plasma distribution (and thus order of the delay) is controlled by the solar activity driven balance of ionization and recombination processes. However, the specific delay is then strongly characterized by the days with enhanced geomagnetic activity
3. O^+ and O_2^+ densities define N_e and thus cause different delays for N_e at heights with their respective peaks (see Figure 6). For this reason, strong variations are observed for the height-dependent delayed ionospheric response
4. O_2^+ densities are decreased due to the accumulation of O^+, but also the O and O_2 are affected (see Figure 7). Photodissociation of O_2 until the second half of the 27-day solar rotation period causes increased Ψ_O and decreased Ψ_{O_2}. This confirms the influence of this process identified in previous studies (Jakowski et al., 1991; Vaishnav et al., 2021)

TIE-GCM runs based on artificial solar activity input (see Figures 9 and 10) were used to show the the impact of the involved processes more clearly and to discuss the impact of transport processes:

1. The conclusions of the first TIE-GCM run are confirmed and Figure 9 illustrates in more detail the contribution of O^+ and O_2^+ densities to the delayed ionospheric response (without impact of geomagnetic activity)

2. O^+ accumulation is strong at the N_e peak (at ∼270 km), but the accumulation persists for the longest time at heights from 180 to 200 km
3. Ψ_O and Ψ_{O_2} show significantly stronger shifts of the 27-day signature than the ionized parts
4. Different delays are observed for upward and downward winds. Upward winds are increased during the first half of the 27-day solar rotation period, while downward winds dominate during the second half. Due to this feature, the original state of the ionosphere is recovered after the 27 days
5. The effectiveness of transport processes is also dependent on the distance between the peaks of O^+ and O_2^+, which is for this reason also a crucial factor for the balance of ionization and recombination

The height-dependent analysis of the delayed ionospheric response shows that investigations based on integral measurements (e.g., TEC) or without considering thermospheric contributions is not sufficient. The delay obtained for the entire ionosphere is driven by several processes depending on the height in the upper atmosphere and the solar EUV spectrum (see Figure 13). For this reason, future analyses should include those observations that provide insight into these processes.

Statistically significant results can be obtained by applying SEA. This method was applied to foF2 and hmF2 in Section 5.2 to describe the delayed response (see Figure 15). In the future, the proposed method may be performed as a function of height to remove, e.g., geomagnetic activity impacts.

Finally, the coupling of MLT and a possible relation in the occurring phase shifts to solar activity in both regions were discussed (see Section 5.3). Future analysis of this interaction could be realized using measurement data (e.g., GOLD and ICON) or realized using models that cover the combined height range (e.g., TIME-GCM and WACCM-X).

Data Availability Statement

The OMNI data were obtained from the GSFC/SPDF OMNIWeb interface at https://omniweb.gsfc.nasa.gov/. The Bremen Mg II composite data were obtained from the UVSat interface at http://www.iup.uni-bremen.de/UVSAT/datasets/mgii/. Information on the Mg II data can be found in Snow et al. (2014). The Kp index data were obtained from the GFZ Potsdam interface at https://www.gfz-potsdam.de/kp-index/. The ionosonde data were obtained from the NOAA NCEI repository at https://data.ngdc.noaa.gov/instruments/remote-sensing/active/profilers-sounders/ionosonde/data/. Data of the TIE-GCM run for the comparison with ionosonde data are provided at https://doi.org/10.5281/zenodo.5937700. Data of the TIE-GCM run using artificial inputs are provided at https://doi.org/10.5281/zenodo.5937462.

Acknowledgments
The authors thank the following institutions for making the various data sets publicly available: NASA/GSFC for providing the OMNI data, IUP Bremen for providing the Mg II composite data, GFZ Potsdam for providing the Kp index, NOAA/NCEI for providing the ionosonde data, and HAO/NCAR for providing TIE-GCM. Open access funding enabled and organized by Projekt DEAL.

References

Afraimovich, E. L., Astafyeva, E. I., Oinats, A. V., Yasukevich, Y. V., & Zhivetiev, I. V. (2008). Global electron content: A new conception to track solar activity. *Annales Geophysicae*, *26*(2), 335–344. https://doi.org/10.5194/angeo-26-335-2008

Cai, X., Burns, A. G., Wang, W., Qian, L., Solomon, S. C., Eastes, R. W.,et al. (2020). The two-dimensional evolution of thermospheric ∑o/n 2 response to weak geomagnetic activity during solar-minimum observed by GOLD. *Geophysical Research Letters*, *47*, e2020GL088838. https://doi.org/10.1029/2020GL088838

Cai, X., Burns, A. G., Wang, W., Qian, L., Solomon, S. C., Eastes, R. W.,et al. (2021). Investigation of a neutral "tongue" observed by GOLD during the geomagnetic storm on May 11, 2019. *Journal of Geophysical Research: Space Physics*, *126*, e2020JA028817. https://doi.org/10.1029/2020JA028817

Chang, L. C., Lin, C.-H., Liu, J.-Y., Balan, N., Yue, J., & Lin, J.-T. (2013). Seasonal and local time variation of ionospheric migrating tides in 2007-2011 FORMOSAT-3/COSMIC and TIE-GCM total electron content. *Journal of Geophysical Research: Space Physics*, *118*, 2545–2564. https://doi.org/10.1002/jgra.50268

DeLand, M. T., & Cebula, R. P. (1993). Composite Mg II solar activity index for solar cycles 21 and 22. *Journal of Geophysical Research*, *98*(D7), 12809. https://doi.org/10.1029/93JD00421

Dyrland, M. E., & Sigernes, F. (2007). An update on the hydroxyl airglow temperature record from the auroral station in Adventdalen, Svalbard (1980–2005). *Canadian Journal of Physics*, *85*(2), 143–151. https://doi.org/10.1139/p07-040

Fioletov, V. E. (2009). Estimating the 27-day and 11-year solar cycle variations in tropical upper stratospheric ozone. *Journal of Geophysical Research*, *114*, D02302. https://doi.org/10.1029/2008JD010499

GFZ. (2021). *Geomagnetic Kp index*. Retrieved from https://www.gfz-potsdam.de/kp-index/

Hagan, M. E., & Forbes, J. M. (2002). Migrating and nonmigrating diurnal tides in the middle and upper atmosphere excited by tropospheric latent heat release. *Journal of Geophysical Research: Atmospheres*, *107*(D24), 4754. https://doi.org/10.1029/2001JD001236

Hagan, M. E., & Forbes, J. M. (2003). Migrating and nonmigrating semidiurnal tides in the upper atmosphere excited by tropospheric latent heat release. *Journal of Geophysical Research*, *108*(A2), 1062. https://doi.org/10.1029/2002JA009466

HAO.(2021).*Thermosphere ionosphere electrodynamics general circulation model*.Retrievedfromhttps://www.hao.ucar.edu/modeling/tgcm/tie.php

Harding, B. J., Makela, J. J., Englert, C. R., Marr, K. D., Harlander, J. M., England, S. L., & Immel, T. J. (2017). The MIGHTI wind retrieval algorithm: Description and verification. *Space Science Reviews*, *212*(1–2), 585–600. https://doi.org/10.1007/s11214-017-0359-3

Heelis, R. A., Lowell, J. K., & Spiro, R. W. (1982). A model of the high-latitude ionospheric convection pattern. *Journal of Geophysical Research*, *87*(A8), 6339. https://doi.org/10.1029/JA087iA08p06339

Hood, L. L. (1986). Coupled stratospheric ozone and temperature responses to short-term changes in solar ultraviolet flux: An analysis of Nimbus 7 SBUV and SAMS data. *Journal of Geophysical Research*, *91*(D4), 5264. https://doi.org/10.1029/JD091iD04p05264

Huang, J., Hao, Y., Zhang, D., & Xiao, Z. (2016). Changes of solar extreme ultraviolet spectrum in solar cycle 24. *Journal of Geophysical Research: Space Physics*, *121*, 6844–6854. https://doi.org/10.1002/2015JA022231

IUP. (2021). *Observations of solar activity by GOME, SCIAMACHY, and GOME-2*. Retrieved from http://www.iup.uni-bremen.de/UVSAT/Datasets/mgii

Jakowski, N., Fichtelmann, B., & Jungstand, A. (1991). Solar activity control of ionospheric and thermospheric processes. *Journal of Atmospheric and Terrestrial Physics*, *53*(11), 1125–1130. https://doi.org/10.1016/0021-9169(91)90061-B

Jakowski, N., Heise, S., Wehrenpfennig, A., Schlüter, S., & Reimer, R. (2002). GPS/GLONASS-based TEC measurements as a contributor for space weather forecast. *Journal of Atmospheric and Solar-Terrestrial Physics*, *64*(5–6), 729–735. https://doi.org/10.1016/s1364-6826(02)00034-2

Kelley, M. (2009). *The Earth's ionosphere* (Vol. 96). Academic Press. https://doi.org/10.1016/B978-0-12-404013-7.X5001-1

Laštovička, J. (2006). Forcing of the ionosphere by waves from below. *Journal of Atmospheric and Solar-Terrestrial Physics*, *68*(3–5), 479–497. https://doi.org/10.1016/j.jastp.2005.01.018

Lednyts'kyy, O., von Savigny, C., & Weber, M. (2017). Sensitivity of equatorial atomic oxygen in the MLT region to the 11-year and 27-day solar cycles. *Journal of Atmospheric and Solar-Terrestrial Physics*, *162*, 136–150. https://doi.org/10.1016/j.jastp.2016.11.003

Lee, C.-K., Han, S.-C., Bilitza, D., & Seo, K.-W. (2012). Global characteristics of the correlation and time lag between solar and ionospheric parameters in the 27-day period. *Journal of Atmospheric and Solar-Terrestrial Physics*, *77*, 219–224. https://doi.org/10.1016/j.jastp.2012.01.010

Liu, J., Wang, W., Burns, A., Solomon, S. C., Zhang, S., Zhang, Y., & Huang, C. (2016). Relative importance of horizontal and vertical transports to the formation of ionospheric storm-enhanced density and polar tongue of ionization. *Journal of Geophysical Research: Space Physics*, *121*, 8121–8133. https://doi.org/10.1002/2016JA022882

Ma, R., Xu, J., Wang, W., & Lei, J. (2012). The effect of ~27 day solar rotation on ionospheric F2 region peak densities (NmF2). *Journal of Geophysical Research*, *117*, A03303. https://doi.org/10.1029/2011JA017190

Matzka, J., Bronkalla, O., Tornow, K., Elger, K., & Stolle, C. (2021). *Geomagnetic Kp index. v. 1.0. GFZ data services*. https://doi.org/10.5880/Kp.0001

Matzka, J., Stolle, C., Yamazaki, Y., Bronkalla, O., & Morschhauser, A. (2021). The geomagnetic Kp index and derived indices of geomagnetic activity. *Space Weather*, *19*, e2020SW002641. https://doi.org/10.1029/2020SW002641

Maute, A. (2017). Thermosphere-ionosphere-electrodynamics general circulation model for the ionospheric connection explorer: TIEGCM-ICON. *Space Science Reviews*, *212*(1–2), 523–551. https://doi.org/10.1007/s11214-017-0330-3

McKinnell, L. (2008). The progress of the South African ionosonde network. *AIP Conference Proceedings*, *974*(1), 47–51. https://doi.org/10.1063/1.2885032

Min, K., Park, J., Kim, H., Kim, V., Kil, H., Lee, J., et al. (2009). The 27-day modulation of the low-latitude ionosphere during a solar maximum. *Journal of Geophysical Research: Space Physics*, *114*, A04317. https://doi.org/10.1029/2008JA013881

NASA. (2021). *NASA/GSFC's OMNIWeb interface*. Retrieved from https://omniweb.gsfc.nasa.gov/form/dx1.html

NCEI. (2021). *Vertical ionograms*. Retrieved from https://data.ngdc.noaa.gov/instruments/remote-sensing/active/profilers-sounders/ionosonde/data/

Oinats, A. V., Ratovsky, K. G., & Kotovich, G. V. (2008). Influence of the 27-day solar flux variations on the ionosphere parameters measured at Irkutsk in 2003–2005. *Advances in Space Research*, *42*(4), 639–644. https://doi.org/10.1016/j.asr.2008.02.009

Qian, L., Burns, A. G., Emery, B. A., Foster, B., Lu, G., Maute, A.,et al. (2014). The NCAR TIE-GCM. In *Modeling the ionosphere-thermosphere system* (pp. 73–83). John Wiley & Sons, Ltd. https://doi.org/10.1002/9781118704417.ch7

Qian, L., Burns, A. G., Solomon, S. C., & Wang, W. (2013). Annual/semiannual variation of the ionosphere. *Geophysical Research Letters*, *40*, 1928–1933. https://doi.org/10.1002/grl.50448

Qian, L., Solomon, S. C., & Kane, T. J. (2009). Seasonal variation of thermospheric density and composition. *Journal of Geophysical Research*, *114*, A01312. https://doi.org/10.1029/2008JA013643

Ren, D., Lei, J., Wang, W., Burns, A., & Luan, X. (2021). Observations and simulations of the peak response time of thermospheric mass density to the 27-day solar EUV flux variation. *Journal of Geophysical Research: Space Physics*, *126*, e2020JA028756. https://doi.org/10.1029/2020JA028756

Ren, D., Lei, J., Wang, W., Burns, A., Luan, X., & Dou, X. (2018). Does the peak response of the ionospheric F2 region plasma lag the peak of 27-day solar flux variation by multiple days? *Journal of Geophysical Research: Space Physics*, *123*, 7906–7916. https://doi.org/10.1029/2018JA025835

Ren, D., Lei, J., Wang, W., Burns, A., Luan, X., & Dou, X. (2019). A simulation study on the time delay of daytime thermospheric temperature response to the 27-day solar EUV flux variation. *Journal of Geophysical Research: Space Physics*, *124*, 9184–9193. https://doi.org/10.1029/2019JA027000

Ren, D., Lei, J., Wang, W., Burns, A., Luan, X., & Dou, X. (2020). Different peak response time of daytime thermospheric neutral species to the 27-day solar EUV flux variations. *Journal of Geophysical Research: Space Physics*, *125*, e2020JA027840. https://doi.org/10.1029/2020JA027840

Rishbeth, H. (1998). How the thermospheric circulation affects the ionospheric F2-layer. *Journal of Atmospheric and Solar-Terrestrial Physics*, *60*(14), 1385–1402. https://doi.org/10.1016/S1364-6826(98)00062-5

Rishbeth, H., & Mendillo, M. (2001). Patterns of F2-layer variability. *Journal of Atmospheric and Solar-Terrestrial Physics*, *63*(15), 1661–1680. https://doi.org/10.1016/S1364-6826(01)00036-0

Robert, C. E., von Savigny, C., Rahpoe, N., Bovensmann, H., Burrows, J. P., DeLand, M. T., & Schwartz, M. J. (2010). First evidence of a 27 day solar signature in noctilucent cloud occurrence frequency. *Journal of Geophysical Research*, *115*, D00I12. https://doi.org/10.1029/2009JD012359

Roble, R. G., & Ridley, E. C. (1987). An auroral model for the NCAR thermospheric general circulation model (TGCM). *Annales Geophysicae*, *5*, 369–382.

Roble, R. G., Ridley, E. C., Richmond, A. D., & Dickinson, R. E. (1988). A coupled thermosphere/ionosphere general circulation model. *Geophysical Research Letters*, *15*(12), 1325–1328. https://doi.org/10.1029/GL015i012p01325

Rong, P., von Savigny, C., Zhang, C., Hoffmann, C. G., & Schwartz, M. J. (2020). Response of middle atmospheric temperature to the 27 d solar cycle: An analysis of 13 years of microwave limb sounder data. *Atmospheric Chemistry and Physics*, *20*(3), 1737–1755. https://doi.org/10.5194/acp-20-1737-2020

Salinas, C. C. J. H., Chang, L. C., Liang, M.-C., Yue, J., Russell, J., & Mlynczak, M. (2016). Impacts of SABER CO_2-based eddy diffusion coefficients in the lower thermosphere on the ionosphere/thermosphere. *Journal of Geophysical Research: Space Physics*, *121*, 12080–12092. https://doi.org/10.1002/2016JA023161

Schmölter, E., Berdermann, J., & Codrescu, M. (2021). The delayed ionospheric response to the 27-day solar rotation period analyzed with GOLD and IGS TEC data. *Journal of Geophysical Research: Space Physics*, *126*, e2020JA028861. https://doi.org/10.1029/2020JA028861

Schmölter, E., Berdermann, J., Jacobi, C., & Jakowski, N. (2020). Modeling of the delayed ionospheric response with the TIE-GCM model. In *2020 European Navigation Conference (ENC)* (pp. 1–9). https://doi.org/10.23919/ENC48637.2020.9317355

Schmölter, E., Berdermann, J., Jakowski, N., & Jacobi, C. (2020). Spatial and seasonal effects on the delayed ionospheric response to solar EUV changes. *Annales Geophysicae*, *38*(1), 149–162. https://doi.org/10.5194/angeo-38-149-2020

Schmölter, E., Berdermann, J., Jakowski, N., Jacobi, C., & Vaishnav, R. (2018). Delayed response of the ionosphere to solar EUV variability. *Advances in Radio Science*, *16*, 149–155. https://doi.org/10.5194/ars-16-149-2018

Snow, M., Weber, M., Machol, J., Viereck, R., & Richard, E. (2014). Comparison of Magnesium II core-to-wing ratio observations during solar minimum 23/24. *Journal of Space Weather and Space Climate*, *4*, A04. https://doi.org/10.1051/swsc/2014001

Solomon, S. C. (2005). Solar extreme-ultraviolet irradiance for general circulation models. *Journal of Geophysical Research*, *110*, A10306. https://doi.org/10.1029/2005JA011160

Sutton, E. K., Thayer, J. P., Wang, W., Solomon, S. C., Liu, X., & Foster, B. T. (2015). A self-consistent model of helium in the thermosphere. *Journal of Geophysical Research: Space Physics*, *120*, 6884–6900. https://doi.org/10.1002/2015JA021223

Tapping, K. F. (2013). The 10.7 cm solar radio flux (F10.7). *Space Weather*, *11*, 394–406. https://doi.org/10.1002/swe.20064

Thomas, G. E., Thurairajah, B., Hervig, M. E., von Savigny, C., & Snow, M. (2015). Solar-induced 27-day variations of mesospheric temperature and water vapor from the AIM SOFIE experiment: Drivers of polar mesospheric cloud variability. *Journal of Atmospheric and Solar-Terrestrial Physics*, *134*, 56–68. https://doi.org/10.1016/j.jastp.2015.09.015

Titheridge, J. E. (1973). The electron content of the southern mid-latitude ionosphere, 1965–1971. *Journal of Atmospheric and Terrestrial Physics*, *35*(5), 981–1001. https://doi.org/10.1016/0021-9169(73)90077-9

Vaishnav, R., Jacobi, C., & Berdermann, J. (2019). Long-term trends in the ionospheric response to solar extreme-ultraviolet variations. *Annales Geophysicae*, *37*(6), 1141–1159. https://doi.org/10.5194/angeo-37-1141-2019

Vaishnav, R., Jacobi, C., Berdermann, J., Codrescu, M., & Schmölter, E. (2021). Role of eddy diffusion in the delayed ionospheric response to solar flux changes. *Annales Geophysicae*, *39*(4), 641–655. https://doi.org/10.5194/angeo-39-641-2021

Vaishnav, R., Jacobi, C., Berdermann, J., Schmölter, E., & Codrescu, M. (2018). Ionospheric response to solar EUV variations: Preliminary results. *Advances in Radio Science*, *16*, 157–165. https://doi.org/10.5194/ars-16-157-2018

Vaishnav, R., Schmölter, E., Jacobi, C., Berdermann, J., & Codrescu, M. (2020). Ionospheric response to solar EUV radiation variations: Comparison based on CTIPe model simulations and satellite measurements. *Annales Geophysicae*, 1–24. https://doi.org/10.5194/angeo-2020-83

Viereck, R., Puga, L., McMullin, D., Judge, D., Weber, M., & Tobiska, W. K. (2001). The Mg II index: A proxy for solar EUV. *Geophysical Research Letters*, *28*(7), 1343–1346. https://doi.org/10.1029/2000GL012551

Vincent, R. A. (2015). The dynamics of the mesosphere and lower thermosphere: A brief review. *Progress in Earth and Planetary Science*, *2*(1), 4. https://doi.org/10.1186/s40645-015-0035-8

von Savigny, C., Eichmann, K.-U., Robert, C. E., Burrows, J. P., & Weber, M. (2012). Sensitivity of equatorial mesopause temperatures to the 27-day solar cycle. *Geophysical Research Letters*, *39*, L21804. https://doi.org/10.1029/2012GL053563

von Savigny, C., Peters, D. H. W., & Entzian, G. (2019). Solar 27-day signatures in standard phase height measurements above central Europe. *Atmospheric Chemistry and Physics*, *19*(3), 2079–2093. https://doi.org/10.5194/acp-19-2079-2019

Wang, S., Zhang, Q., Millán, L., Li, K.-F., Yung, Y. L., Sander, S. P.,et al. (2015). First evidence of middle atmospheric HO2response to 27 day solar cycles from satellite observations. *Geophysical Research Letters*, *42*, 10004–10009. https://doi.org/10.1002/2015GL065237

Wu, Q., Schreiner, W. S., Ho, S.-P., Liu, H.-L., & Qian, L. (2017). Observations and simulations of eddy diffusion and tidal effects on the semiannual oscillation in the ionosphere. *Journal of Geophysical Research: Space Physics*, *122*, 10502–10510. https://doi.org/10.1002/2017JA024341

Yu, T., Wang, W., Ren, Z., Cai, X., Yue, X., & He, M. (2021). The response of middle thermosphere (∼160 km) composition to the November 20 and 21, 2003 superstorm. *Journal of Geophysical Research: Space Physics*, *126*, e2021JA029449. https://doi.org/10.1029/2021JA029449

Zhang, S.-R., & Holt, J. M. (2008). Ionospheric variability from an incoherent scatter radar long-duration experiment at Millstone Hill. *Journal of Geophysical Research: Space Physics*, *113*, A03310. https://doi.org/10.1029/2007JA012639

Zhao, Y., Taylor, M. J., Pautet, P.-D., Moffat-Griffin, T., Hervig, M. E., Murphy, D. J.,et al. (2019). Investigating an unusually large 28-day oscillation in mesospheric temperature over Antarctica using ground-based and satellite measurements. *Journal of Geophysical Research: Atmospheres*, *124*, 8576–8593. https://doi.org/10.1029/2019JD030286

Zhou, X., Yue, X., Liu, H.-L., Lu, X., Wu, H., Zhao, X., & He, J. (2021). A comparative study of ionospheric day-to-day variability over Wuhan based on ionosonde measurements and model simulations. *Journal of Geophysical Research: Space Physics*, *126*, e2020JA028589. https://doi.org/10.1029/2020JA028589